Imaging with the elliptic Radon transform in 3D from an analytical and numerical perspective

Christine Grathwohl, Peer Christian Kunstmann,
Eric Todd Quinto, Andreas Rieder

KARLSRUHE INSTITUTE OF TECHNOLOGY

CRC 1173

WaVe
phenomena

Participating universities

Universität Stuttgart

EBERHARD KARLS
UNIVERSITÄT
TÜBINGEN

TU
WIEN

Funded by

DFG

IMAGING WITH THE ELLIPTIC RADON TRANSFORM IN 3D FROM AN ANALYTICAL AND NUMERICAL PERSPECTIVE

CHRISTINE GRATHWOHL, PEER CHRISTIAN KUNSTMANN, ERIC TODD QUINTO,
AND ANDREAS RIEDER

ABSTRACT. The three-dimensional elliptic Radon transform (eRT) averages distributions over ellipsoids of revolution. It thus serves as a linear model in seismic imaging where one wants to recover the earth's interior from reflected wave fields. As there is no inversion formula known for the eRT, approximate formulas have to be used. In this paper we suggest several of those, microlocally analyze their properties, provide and implement an adapted algorithm whose performance we test by diverse numerical experiments. Our previous results of [*Inverse Problems, 34 (2018), 014002 & 114001*] are thus generalized to three space dimensions.

1. INTRODUCTION

The elliptic Radon transform F serves as a model in seismic imaging when sources and receivers are offset by a constant vector and linearization has been performed about a constant background sound speed. One is led to solve the linear equation $Fn = y$ where y represents pre-processed measurements of the reflected acoustic wave fields and n represents the high frequency content of the searched-for true speed of sound. As there is no inversion formula known in this geometric setting, one has to find, study, and implement more general approximate inversion schemes.

For instance, in Kirchhoff migration, the classical inversion scheme of geophysics, one applies a kind of convolution operator K followed by a dual transform (generalised backprojection) $F^\sharp$ to the data to obtain $F^\sharp Ky$. Instead of n we thus recover $F^\sharp KFn$. The *imaging operator* $F^\sharp KF$ is the sum of a low pass filter (partial identity) and a smoothing operator, see [3]. Consequently, some of the features of n are indeed visible in $F^\sharp KFn$.

Another approach consists of applying F^*, the formal L^2-adjoint (backprojection), yielding the normal operator $F^*\psi F$ as imaging operator (ψ is a smooth cutoff function needed for technical reasons, see start of Section 3 below). Imaging properties of $F^*\psi F$ in different settings have been analyzed by many authors including [7, 8, 17, 21, 23].

In our two previous papers [11, 12] (see also [20]) we have contributed to this research twofold: First, we have augmented the normal operator by a properly supported pseudodifferential operator K of positive order so that $KF^*\psi F$ enhances features (discontinuities) of n. In contrast, the abovementioned two examples deliver rather smooth

versions of n. Further, we have microlocally analyzed these operators in two spatial dimensions to understand how they map singularities. Using this knowledge, we have been able to construct K with useful imaging properties. Second, also in two spatial dimensions, we have developed and implemented a corresponding regularization scheme based on the approximate inverse [16]. The present paper extends our two dimensional results to three space dimensions. By no means is this generalization trivial: the microlocal analysis is more involved and the implementation of the numerical scheme poses additional challenges.

Our material is organized as follows. In the next section we shortly recall how the seismic model with the elliptic Radon transform is obtained by linearizing the acoustic wave equation. Then, we introduce our first imaging operator in Section 3, analyze it microlocally which leads us to define new operators with improved imaging properties. For a rather self-contained presentation we provide basic concepts from microlocal analysis. Section 4 is devoted to our numerical scheme where implementation issues are discussed in some detail. Finally, we report and comment on numerical experiments not only to illustrate our microlocal predictions (Section 5.1) but also to test the robustness of the numerical scheme with respect to noise in the offset and modeling error (Section 5.2). Moreover, we discuss the formation of artifacts appearing in the reconstructions. A sound microlocal explanation remains to be given, though, in future research.

2. The forward operator

A well-established method to investigate the subsurface of the earth is to generate pressure waves on the surface and measure their returning reflections. For simplification we assume that no shear waves occur and that the earth has constant mass density. Then, wave propagation with sound speed ν is described by the acoustic wave equation

$$(2.1) \qquad \frac{1}{\nu^2(x)}\partial_t^2 u(t,x;\mathbf{x}_\mathrm{s}) - \Delta u(t,x;\mathbf{x}_\mathrm{s}) = \delta(x - \mathbf{x}_\mathrm{s})\delta(t)$$

for time $t \geq 0$ at location $x \in \mathbb{R}^3$ with source location $\mathbf{x}_\mathrm{s}$. We augment (2.1) with vanishing initial conditions

$$(2.2) \qquad u(0,\,\cdot\,;\mathbf{x}_\mathrm{s}) = \partial_t u(0,\,\cdot\,;\mathbf{x}_\mathrm{s}) = 0$$

(interpreted in a distributional sense) since the environment is at rest before the wave is excited. The task is to reconstruct the speed of sound ν from the backscattered field $u(t,\mathbf{x}_\mathrm{r};\mathbf{x}_\mathrm{s})$ observed at a receiver point $\mathbf{x}_\mathrm{r}$ for $(t,\mathbf{x}_\mathrm{r};\mathbf{x}_\mathrm{s}) \in [0,T_\mathrm{max}] \times \mathcal{R} \times \mathcal{S}$ where T_max is the recording time and $\mathcal{R}$ and $\mathcal{S}$ are the sets of receiver and source positions, respectively.

We consider the common offset scanning geometry where the distance of source to receiver is a constant vector. This geometry is realized by

$$\mathbf{x}_\mathrm{s} = \mathbf{x}_\mathrm{s}(s) = (s_1, s_2 - \alpha, 0)^\top \quad \text{and } \mathbf{x}_\mathrm{r} = \mathbf{x}_\mathrm{r}(s) = (s_1, s_2 + \alpha, 0)^\top$$

for a fixed offset $\alpha \geq 0$ and $(s_1, s_2) \in S_0 \subseteq \mathbb{R}^2$, where S_0 is a non-empty open, bounded and connected subset of $\mathbb{R}^2$.

To solve the inverse problem, we make the classical ansatz

$$\frac{1}{\nu^2(x)} = \frac{1 + n(x)}{c^2}$$

for $x \in \mathbb{R}^3$ with a constant and priori known background velocity c, say $c = 1$, and a function n being compactly supported in $\mathbb{R}_+^3 := \{x \in \mathbb{R}^3 \,|\, x_3 > 0\}$ (the x_3-axis points

downwards). In doing so we are seeking n instead of ν. Physically the quantity n can be interpreted as a kind of reflectivity, which captures the high frequency variations of ν, see [4, Sec. 3.2.1].

The solution $\widetilde{u}$ of (2.1) and (2.2) for $\nu = c = 1$ is our reference solution:

$$(2.3) \qquad \partial_t^2 \widetilde{u}(t, x; \mathbf{x}_{\mathrm{s}}(s)) - \Delta \widetilde{u}(t, x; \mathbf{x}_{\mathrm{s}}(s)) = \delta(x - \mathbf{x}_{\mathrm{s}}(s))\delta(t).$$

We follow the lines of [6] and [24] to derive a linear equation for n. For further details see [10] and [12].

By the Born approximation we derive the following representation of $u - \widetilde{u}$:

$$(2.4) \quad (u - \widetilde{u})(t, \mathbf{x}_{\mathrm{r}}(s); \mathbf{x}_{\mathrm{s}}(s))$$
$$= -\partial_t^2 \int_{\mathbb{R}_+^3} a_{\mathbf{x}_{\mathrm{s}}(s)}(x) a_{\mathbf{x}_{\mathrm{r}}(s)}(x) n(x) \delta(t - \tau_{\mathbf{x}_{\mathrm{s}}(s)}(x) - \tau_{\mathbf{x}_{\mathrm{r}}(s)}(x)) \, \mathrm{d}x$$

with

$$a_y(x) = \frac{1}{4\pi|x - y|} \qquad \text{and} \qquad \tau_y(x) = |x - y|.$$

Using the abbreviations

$$A(s, x) := 16\pi^2 a_{\mathbf{x}_{\mathrm{s}}(s)}(x) a_{\mathbf{x}_{\mathrm{r}}(s)}(x) = \frac{1}{|\mathbf{x}_{\mathrm{s}}(s) - x||x - \mathbf{x}_{\mathrm{r}}(s)|}$$

and

$$\varphi(s, x) := \tau_{\mathbf{x}_{\mathrm{s}}(s)}(x) + \tau_{\mathbf{x}_{\mathrm{r}}(s)}(x) = |\mathbf{x}_{\mathrm{s}}(s) - x| + |x - \mathbf{x}_{\mathrm{r}}(s)|,$$

we define the operator

$$Fn(s, t) := \int_{\mathbb{R}_+^3} n(x) A(s, x) \delta(t - \varphi(s, x)) \, \mathrm{d}x, \quad (s, t) \in S_0 \times (2\alpha, \infty).$$

Next, we integrate (2.4) two times with respect to t to get

$$Fn(s, t) = y(s, t)$$

with right hand side

$$(2.5) \qquad y(s, t) = -16\pi^2 \int_0^t (t - r)(u - \widetilde{u})(r, \mathbf{x}_{\mathrm{r}}(s); \mathbf{x}_{\mathrm{s}}(s)) \, \mathrm{d}r,$$

which is known from the measurements and from the reference solution (2.3).

Note that F is a generalized Radon transform which integrates over open half ellipsoids

$$E(s, t) = \{x \in \mathbb{R}_+^3 \mid \varphi(s, x) = t\} = \{x \in \mathbb{R}_+^3 \mid |\mathbf{x}_{\mathrm{s}}(s) - x| + |x - \mathbf{x}_{\mathrm{r}}(s)| = t\}.$$

We refer to [19, Def. 2.1] for the definition of generalized Radon transforms. More details are given in [10, Sec. 3.1]. Moreover, F is a Fourier integral operator (see [14] for the definition), which can be written as

$$(2.6) \qquad Ff(s, t) = \int_{\mathbb{R}_+^3} f(x)\delta(t - \varphi(s, x)) A(s, x) \, \mathrm{d}x$$
$$= \frac{1}{2\pi} \int_{\mathbb{R}} \int_{\mathbb{R}_+^3} f(x) A(s, x) \mathrm{e}^{\mathrm{i}\omega(t - \varphi(s, x))} \, \mathrm{d}x \, \mathrm{d}\omega$$

for $f \in C_c^\infty(\mathbb{R}_+^3)$. The functions $(s, t, x, \omega) \mapsto \frac{1}{2\pi} A(s, x)$ for $(s, t, x, \omega) \in S_0 \times (2\alpha, \infty) \times \mathbb{R}_+^3 \times \mathbb{R}$ and $(s, t, x, \omega) \mapsto \omega(t - \varphi(s, x))$ are the symbol and the phase of F, respectively.

3. Imaging

To the best of our knowledge there is no formula known to reconstruct n directly from the elliptic means $g = Fn$ in case $\alpha > 0$. Therefore, we define the imaging operator

$$(3.1) \qquad \Lambda := -\Delta \partial_3 F^* \psi F,$$

which was introduced in [20] for $\alpha = 0$ based on an inversion formula of [1]. So, instead of n we are able to reconstruct at least Λn from g. Here, Δ is the Laplace operator, ∂_3 the derivative in third space direction (downwards), and ψ is a function in $C_c^\infty(S_0 \times (2\alpha, \infty))$. Further, F^* is dual to F and given by

$$(3.2) \qquad F^* g(x) = \int_{S_0 \times (2\alpha,\infty)} g(s,t) \delta(t - \varphi(s,x)) A(s,x) \, \mathrm{d}(s,t)$$

$$= \frac{1}{2\pi} \int_{\mathbb{R}} \int_{S_0 \times (2\alpha,\infty)} g(s,t) A(s,x) \mathrm{e}^{\mathrm{i}\omega(t - \varphi(s,x))} \, \mathrm{d}(s,t) \, \mathrm{d}\omega$$

for $g \in C_c^\infty(S_0 \times (2\alpha, \infty))$ and $x \in \mathbb{R}_+^3$. The cutoff function ψ is needed to have a well-defined composition of F^* with F as $F \colon \mathcal{E}'(\mathbb{R}_+^3) \to \mathcal{D}'(S_0 \times (2\alpha, \infty))$ and $F^* \colon \mathcal{E}'(S_0 \times (2\alpha, \infty)) \to \mathcal{D}'(\mathbb{R}_+^3)$. Our Λ is a special case of imaging operators investigated in [12]. Moreover, it is a pseudodifferential operator of order 1 [12, Th. 3.3], which makes it useful for imaging purposes as we explain in the following section.

3.1. **Pseudodifferential Operators and microlocal analysis.** Our theoretical results are based on the theory of pseudodifferential operators and their microlocal properties. The following basic concepts can be found in many textbooks, we refer, e.g., to [18].

Definition 3.1 (Pseudodifferential symbol). Let $d \in \mathbb{N}$ and $X \subseteq \mathbb{R}^d$ be open. A *symbol of order $m \in \mathbb{R}$* is a function $p = p(x, \xi) \in C^\infty(X \times \mathbb{R}^d)$ satisfying: For every compact set $\mathrm{K} \subseteq X$ and for each pair of multi-indices α, β there exists a constant $C = C(\mathrm{K}, \alpha, \beta)$ such that, for all $x \in \mathrm{K}$ and all $\xi \in \mathbb{R}^d$,

$$|D_\xi^\alpha D_x^\beta p(x,\xi)| \le C (1 + |\xi|)^{m - |\alpha|}.$$

The set of symbols of order m on X is denoted by $S^m(X)$.

A symbol $p \in S^m(X)$ is *microlocally elliptic of order m* at $(x_0, \xi_0) \in X \times \mathbb{R}^d \backslash \{0\}$ if there are an open neighborhood U of x_0 in X, a conic neighborhood V of ξ_0 in $\mathbb{R}^d \backslash \{0\}$ and constants $M > 0$ and $C > 0$ such that

$$|p(x,\xi)| \ge C (1 + |\xi|)^m$$

for all $x \in U$ and all $\xi \in V$ with $|\xi| \ge M$.

Note that $S^m(X)$ is the standard symbol class of Hörmander [14, Def. 1.1.1].

Definition 3.2 (Pseudodifferential operator). Let $X \subseteq \mathbb{R}^d$ be open and $m \in \mathbb{R}$. Then, the linear operator $P \colon \mathcal{D}(X) \to \mathcal{E}(X)$ is a *pseudodifferential operator of order m* if there is a pseudodifferential symbol p of order m such that for all $f \in \mathcal{D}(X)$,

$$Pf(y) = \int_{\mathbb{R}^d} \int_X \mathrm{e}^{\mathrm{i}(y - x)\cdot\xi} p(x,\xi) f(x) \, \mathrm{d}x \, \mathrm{d}\xi.$$

The function p is called the *full symbol* of the operator P. The *principal symbol $\sigma(P)$ of P* is the equivalence class of p in the quotient space $S^m(X)/S^{m-1}(X)$.

The operator P is *microlocally elliptic* if its symbol is microlocally elliptic.

Please note that the integral defining P in the above definition exists as an *oscillatory integral* and represents a distribution in general [14, Chap. I]. Further, any pseudodifferential operator can be extended as an operator mapping $\mathcal{E}'(X)$ continuously into $\mathcal{D}'(X)$. We tacitly rely on this extension throughout the paper.

Definition 3.3. A function $f\colon \mathbb{R}^d \to \mathbb{C}$ is *rapidly decaying at infinity* on the cone $V \subseteq \mathbb{R}^d$ if for every $N \in \mathbb{N}$ there is a constant $C = C(N) > 0$ such that
$$|f(\xi)| \leq C(1 + |\xi|)^{-N}$$
for all $\xi \in V$.

Definition 3.4. Let $\Omega \subseteq \mathbb{R}^d$ be open. A distribution $u \in \mathcal{D}'(\Omega)$ is *microlocally C^∞* at $(x_0, \xi_0) \in \Omega \times \mathbb{R}^d\backslash\{0\}$ if for some $\phi \in C_c^\infty(\Omega)$ with $\phi(x_0) \neq 0$ and some conic neighborhood V of ξ_0 in $\mathbb{R}^d\backslash\{0\}$, the Fourier transform $\widehat{\phi u}$ is rapidly decaying on V.

As an image carries most of its information content at singularities, we are interested to characterize their location and direction. Those are collected in the *wave front set* of a distribution u:

$$(3.3) \qquad \mathrm{WF}(u) = \{(x, \xi) \in \Omega \times \mathbb{R}^d \setminus \{0\} \,|\, u \text{ is not microlocally } C^\infty \text{ at } (x, \xi)\}.$$

Theorem 3.5 (Pseudolocal property). *If P is a pseudodifferential operator, it holds*
$$\mathrm{WF}(Pu) \subseteq WF(u)$$
for $u \in \mathcal{E}'(\Omega)$. If P is additionally microlocally elliptic at all points $(x, \xi) \in \Omega \times \mathbb{R}^d$, we even obtain the equality
$$\mathrm{WF}(Pu) = WF(u)$$
for $u \in \mathcal{E}'(\Omega)$.

Next, we refine the concept of wave front sets of a distribution by a microlocalization of H^s in lieu of C^∞. A distribution $u \in \mathcal{D}'(\Omega)$ is *microlocally H^r* at $(x_0, \xi_0) \in \Omega \times \mathbb{R}^d\backslash\{0\}$ if for some neighborhood U of x_0 in Ω and some conic neighborhood V of ξ_0 in $\mathbb{R}^d\backslash\{0\}$ we have
$$\int_V |\widehat{\phi u}(\xi)|^2 (1 + |\xi|^2)^r \,\mathrm{d}\xi < \infty$$
for all $\phi \in C_c^\infty(U)$. Now, for $r \in \mathbb{R}$, the *H^r-wave front set* of u is
$$\mathrm{WF}^r(u) = \{(x, \xi) \in \Omega \times \mathbb{R}^d \setminus \{0\} \,|\, u \text{ is not microlocally } H^r \text{ at } (x, \xi)\}.$$

Theorem 3.6. *Let P be a pseudodifferential operator of order m. If P is microlocally elliptic at (x_0, ξ_0), we have*
$$(x_0, \xi_0) \in \mathrm{WF}^r(u) \text{ if and only if } (x_0, \xi_0) \in \mathrm{WF}^{r-m}(Pu)$$
for $u \in \mathcal{E}'(\Omega)$ and $r \in \mathbb{R}$.

3.2. The symbols of $F^*\psi F$ and Λ.

To determine the top order symbol of Λ, we investigate the normal operator

$$(3.4) \quad (F^*\psi F n)(x)$$
$$= \frac{1}{2\pi} \int_{\mathbb{R}_+^3} \int_{\mathbb{R}} \int_{\mathbb{R}^2} \psi(s, \varphi(s, x)) A(s, x) A(s, y) n(y) \mathrm{e}^{\mathrm{i}\omega(\varphi(s,x) - \varphi(s,y))} \,\mathrm{d}s \,\mathrm{d}\omega \,\mathrm{d}y$$

for $n \in C_c^\infty(\mathbb{R}_+^3)$ and $x \in \mathbb{R}_+^3$.

Theorem 3.7. *The wave front set* $\mathrm{WF}(F^*\psi F u)$ *satisfies*

$$\mathrm{WF}(F^*\psi F u) \subseteq \{(x,\xi; x,\xi) \in (\mathbb{R}^3_+ \times \mathbb{R}^3 \setminus \{0\}) \times (\mathbb{R}^3_+ \times \mathbb{R}^3 \setminus \{0\}) \,|\, $$
$$\text{there exists } s \in S_0 \text{ and } \omega \neq 0 \text{ such that } \xi = \omega \nabla_x \varphi(s,x)\} \circ \mathrm{WF}(u)$$

for $u \in \mathcal{E}'(\mathbb{R}^3_+)$. *Here, the operation* $\circ$ *denotes the usual composition of general relations.*

One proves Theorem 3.7 analogously to Theorem 4 of [15]. A detailed proof can be found in [10, Th. 3.15].

In [12, Th. 3.5] we proved explicit representations of the top order symbol for a class of operators that includes Λ, and thus Theorem 3.8 below is a special case. However, the proof is rather technical and requires deep knowledge of measure theory and differential geometry. Here, we lay out a different path, which is confined to the theory of pseudodifferential operators. We adapt and extend ideas of [2].

For technical reasons we need to modify $F^*\psi F$ as well as Λ: for $\delta > 0$ define $\zeta_\delta \in C^\infty(\mathbb{R}^3_+, \mathbb{R})$ by

$$\zeta_\delta(y) = 1 \quad \text{if } y_3 \geq 2\delta \qquad \text{and} \qquad \zeta_\delta(y) = 0 \quad \text{if } y_3 < \delta.$$

Then, we set

$$F^*\psi F_\delta := F^*\psi F\zeta_\delta \quad \text{and} \quad \Lambda_\delta := \Lambda\zeta_\delta = -\Delta\partial_3 F^*\psi F_\delta.$$

In view of (3.4) we have

(3.5) $\quad (F^*\psi F_\delta n)(x)$

$$= \frac{1}{2\pi} \int_{\mathbb{R}^3_+} \int_{\mathbb{R}} \int_{\mathbb{R}^2} \psi(s,\varphi(s,x)) A(s,x) A(s,y) \zeta_\delta(y) n(y) \mathrm{e}^{\mathrm{i}\omega(\varphi(s,x)-\varphi(s,y))} \, \mathrm{d}s \, \mathrm{d}\omega \, \mathrm{d}y.$$

Since n is compactly supported in $\mathbb{R}^3_+$, we have $\Lambda_\delta n = \Lambda n$ for δ sufficiently small. Of course, the size of δ depends on n.

We are now ready to present the top order symbol Λ_δ.

Theorem 3.8. *The operator* Λ_δ *is a sum of a pseudodifferential operator and a smoothing operator.*[1]

Let $(x,\xi) \in \mathbb{R}^3_+ \times \mathbb{R}^3$ *with* $\xi_3 \neq 0$. *If there exist* $s \in S_0$ *and* $\omega \in \mathbb{R}\setminus\{0\}$ *such that* $\xi = \omega\nabla_x\varphi(s,x)$, *then*

(3.6) $\qquad \sigma(\Lambda_\delta)(x,\xi) = (2\pi)^5 \mathrm{i}\xi_3|\xi|^2 \dfrac{\psi(s(x,\xi),\varphi(s(x,\xi),x)) A(s(x,\xi),x)^2 \zeta_\delta(x)}{|\omega(x,\xi)|^2 |B(s(x,\xi),x)|}.$

Here,

(3.7) $\qquad\qquad B(s(x,\xi),x) = \det \begin{pmatrix} [\nabla_x\varphi](s(x,\xi),x)^\top \\ [\partial_{s_1}\nabla_x\varphi](s(x,\xi),x)^\top \\ [\partial_{s_2}\nabla_x\varphi](s(x,\xi),x)^\top \end{pmatrix},$

(3.8) $\qquad\qquad \omega(x,\xi) = \dfrac{\xi_3|\mathbf{x}_{\mathrm{s}}(s(x,\xi)) - x||x - \mathbf{x}_{\mathrm{r}}(s(x,\xi))|}{x_3(|\mathbf{x}_{\mathrm{s}}(s(x,\xi)) - x| + |x - \mathbf{x}_{\mathrm{r}}(s(x,\xi))|)},$

---

[1]A smoothing operator maps all compactly supported distributions to C^∞ functions. For the study of singularities, those operators can be neglected.

and

$$s_1(x, \xi) = x_1 - \frac{\xi_1}{\xi_3} x_3,$$

$$s_2(x, \xi) = \begin{cases} x_2 - \frac{1}{2} \frac{\xi_3}{\xi_2} \left(\left(\frac{\xi_2^2 - \xi_1^2}{\xi_3^2} - 1 \right) x_3 + \sqrt{x_3^2 \left(\frac{\xi_1^2 + \xi_2^2}{\xi_3^2} + 1 \right)^2 + 4\alpha^2 \frac{\xi_2^2}{\xi_3^2}} \right), & \text{for } \xi_2 \neq 0, \\ x_2, & \text{for } \xi_2 = 0. \end{cases}$$

If there is no $s \in S_0$ satisfying $\xi = \omega \nabla_x \varphi(s, x)$ for some $\omega \in \mathbb{R} \backslash \{0\}$, we have $\sigma(\Lambda_\delta) = 0$. Moreover, for $(x, \xi) \in \mathbb{R}_+^3 \times \mathbb{R}^3 \backslash \{0\}$ with $\xi_3 = 0$ the top order symbol $\sigma(\Lambda_\delta)$ vanishes as well.

Proof. We only sketch the main steps and refer to [10, Th. 3.21] for the full proof.

First, we apply the transformation $\widetilde{s} = s\omega$ to the integral in (3.5). So, we obtain a representation of $F^* \psi F_\delta$ as a Fourier integral operator depending on x, y, and the phase variable $(\widetilde{s}, \omega)$. Next, we employ the fact that an operator is smoothing if it vanishes in a conic neighborhood of a certain set (see [22, Prop. 2.1b)]). In case of $F^* \psi F_\delta$ this set is characterized by the diagonal $x = y$. Therefore, for an $\varepsilon > 0$ we introduce the cutoff function $\widehat{\zeta}_\varepsilon \in C^\infty(\mathbb{R}_+^3 \times \mathbb{R}_+^3, \mathbb{R})$ with $0 \leq \widehat{\zeta}_\varepsilon \leq 1$,

$$\widehat{\zeta}_\varepsilon(x, y) = 1 \quad \text{if } |x - y| < \varepsilon \qquad \text{and} \qquad \widehat{\zeta}_\varepsilon(x, y) = 0 \quad \text{if } |x - y| > 2\varepsilon.$$

Using this function, we split $F^* \psi F_\delta$ into a sum of a smoothing operator and an operator which, by [22, Th. 19.2], turns out to be a pseudodifferential operator if ε is sufficiently small. Then, we perform the transformation $\xi = \omega \nabla_x \varphi(\widetilde{s}, \omega, x)$, expand the phase function in a Taylor polynomial about x, and introduce several different smooth cutoff functions to show the required assumptions. Finally, we apply expansion (2.1.4) of [14]. $\square$

3.3. Microlocal properties.

To understand how our imaging operator Λ maps, emphasizes or de-emphasizes singularities, we now analyze its top order symbol.

We introduce the ratios

$$p := p(\xi) = \frac{\xi_1}{\xi_3} \quad \text{and} \quad q := q(\xi) = \frac{\xi_2}{\xi_3}$$

for $\xi \in \mathbb{R}^3$ with $\xi_3 \neq 0$ and rewrite $\sigma(\Lambda_\delta)$ in terms of x, ξ_3, p, and q. We find that

$$\{(p, q) \in \mathbb{R}^2 \,|\, \exists \xi \in \mathbb{R}^3, \ \xi_3 \neq 0, \ p = \tfrac{\xi_1}{\xi_3}, \ q = \tfrac{\xi_2}{\xi_3}\} = \mathbb{R}^2.$$

Hence, we consider $(p, q) \in \mathbb{R}^2$ in the following. By Theorem 3.8 we get $s(p, q, x) = (s_1(p, q, x), s_2(p, q, x))$ with

$$s_1(p, q, x) = x_1 - px_3 \quad \text{and} \quad s_2(p, q, x) = x_2 - x_3 Q(p, q, \tfrac{\alpha}{x_3})$$

for $(p, q) \in \mathbb{R}^2$ and $x \in \mathbb{R}_+^3$ where

$$Q(p, q, \lambda) := \begin{cases} \frac{1}{2q} \left(q^2 - p^2 - 1 + \sqrt{(p^2 + q^2 + 1)^2 + 4\lambda^2 q^2} \right), & \text{for } q \neq 0, \\ 0, & \text{for } q = 0, \end{cases}$$

for $(p, q) \in \mathbb{R}^2$ and $\lambda > 0$. Note that s_2 is smooth on its domain of definition [10, Rem. 3.13]. Further,

$$D_+ := D_+(p, q, x) := |x - \mathbf{x}_s(s(p, q, x))| = x_3 \sqrt{(Q(p, q, \tfrac{\alpha}{x_3}) + \tfrac{\alpha}{x_3})^2 + p^2 + 1}$$

and analogously

$$D_- := D_-(p, q, x) = x_3 \sqrt{(Q(p, q, \tfrac{\alpha}{x_3}) - \tfrac{\alpha}{x_3})^2 + p^2 + 1}.$$

With these abbreviations we have

$$A(p, q, x) := A(s(p, q, x), x) = \frac{1}{D_+(p, q, x)} \frac{1}{D_-(p, q, x)}$$

and

$$\psi(p, q, x) := \psi(s(p, q, x), \varphi(s(p, q, x), x)) = D_+(p, q, x) + D_-(p, q, x).$$

By (3.8),

$$\omega(p, q, x, \xi_3) = \frac{\xi_3}{x_3} \frac{D_+(p, q, x) + D_-(p, q, x)}{D_+(p, q, x) D_-(p, q, x)}.$$

From (3.7) we obtain

$$B(s, x) = x_3 \left(\frac{1}{|\mathbf{x}_\mathrm{s}(s) - x|} + \frac{1}{|x - \mathbf{x}_\mathrm{r}(s)|} \right) \left(\frac{1}{|\mathbf{x}_\mathrm{s}(s) - x|^2} + \frac{1}{|x - \mathbf{x}_\mathrm{r}(s)|^2} \right) \left(1 + \frac{x - \mathbf{x}_\mathrm{s}(s)}{|\mathbf{x}_\mathrm{s}(s) - x|} \cdot \frac{x - \mathbf{x}_\mathrm{r}(s)}{|x - \mathbf{x}_\mathrm{r}(s)|} \right)$$

yielding

$$B(p, q, x) = x_3 \left(\frac{1}{D_+(p, q, x)} + \frac{1}{D_-(p, q, x)} \right) \left(\frac{1}{D_+^2(p, q, x)} + \frac{1}{D_-^2(p, q, x)} \right)$$
$$\left(1 + \frac{\left(px_3, x_3 Q\left(p, q, \tfrac{\alpha}{x_3}\right) + \alpha, x_3 \right)^\top}{D_+(p, q, x)} \cdot \frac{\left(px_3, x_3 Q\left(p, q, \tfrac{\alpha}{x_3}\right) - \alpha, x_3 \right)^\top}{D_-(p, q, x)} \right).$$

In our numerical examples of Section 5 below we will only consider functions n with supports a fixed distance away from the surface. This condition is also satisfied in geophysical applications. As a consequence, we need not and we do not distinguish any longer between the operators Λ and Λ_δ.

Proposition 3.9. *Let $(y, \eta) \in \mathbb{R}_+^3 \times \mathbb{R}^3 \backslash \{0\}$ and define*

$$C(y) := \{\xi \in \mathbb{R}^3 \mid \xi_3 \neq 0, \psi(s(y, \xi), \varphi(s(y, \xi), y)) > 0\}.$$

If $\eta \in C(y)$, then Λ is microlocally elliptic of order 1 at (y, η).
Further, Λ is smoothing at $(x, \xi) \in \mathbb{R}_+^3 \times \mathbb{R}^3 \setminus \{0\}$ with $\xi \notin \overline{C(x)}$.

Proof. Let $\eta \in C(y)$. We define $\overline{m} := \eta_1/\eta_3$ and $\overline{n} := \eta_2/\eta_3$, which is possible as η_3 is non-zero. Further, the cutoff function ψ in the definition of the set $C(y)$ is continuous. Thus, there exist $\delta > 0$ and $r > 0$ such that we have

$$\overline{B_r(y)} \subseteq \mathbb{R}_+^3 \quad \text{and} \quad \psi(p, q, x) > 0$$

for $p \in \overline{B_\delta(\overline{m})}$, $q \in \overline{B_\delta(\overline{n})}$ and $x \in \overline{B_r(y)}$.
    In case of $\eta_3 > 0$, we define

$$V_\delta(\eta) := \{(\lambda m, \lambda n, \lambda)^\top \in \mathbb{R}^3 \mid \overline{m} - \delta \leq m \leq \overline{m} + \delta, \overline{n} - \delta \leq n \leq \overline{n} + \delta, \lambda \geq 0\}$$

and for $\eta_3 < 0$ we consider

$$V_\delta(\eta) := \{(-\lambda m, -\lambda n, -\lambda)^\top \in \mathbb{R}^3 \mid \overline{m} - \delta \leq m \leq \overline{m} + \delta, \overline{n} - \delta \leq n \leq \overline{n} + \delta, \lambda \geq 0\}.$$

In both cases, $V_\delta(\eta)$ is a conic neighborhood of η.

In the beginning of this section we have seen that nearly all terms of the symbol depend solely on the two ratios p and q. Hence, we introduce the set

$$M := \big\{ (p, q, x) \in \mathbb{R} \times \mathbb{R} \times \mathbb{R}_+^3 \, | $$

$$\text{there exists } \xi \in V_\delta(\eta) \backslash \{0\}, \ p = \xi_1/\xi_3, \ q = \xi_2/\xi_3 \text{ and } x \in \overline{B_r(y)} \big\}$$

$$= \{ (p, q, x) \in \mathbb{R} \times \mathbb{R} \times \mathbb{R}_+^3 \, | \, \overline{m} - \delta \le p \le \overline{m} + \delta, \overline{n} - \delta \le q \le \overline{n} + \delta, \text{ and } x \in \overline{B_r(y)} \},$$

which is obviously closed and bounded and thus, a compact subset of $\mathbb{R}^5$.

According to Theorem 3.8 we have

$$\sigma(F^*\psi F) = \frac{(2\pi)^5 (D_+(p,q,x) + D_-(p,q,x))^2 \psi(s(p,q,x), \varphi(s(p,q,x), x)) x_3^2}{D_+(p,q,x)^4 D_-(p,q,x)^4 |B(p,q,x)|} \frac{1}{\xi_3^2}$$

for $(p, q, x) \in M$ and ξ_3 such that $\xi \in V_\delta(\eta) \backslash \{0\}$ holds. The map

$$G \colon M \ni (p, q, x) \mapsto \left| \frac{(2\pi)^5 (D_+(p,q,x) + D_-(p,q,x))^2 \psi(s(p,q,x), \varphi(s(p,q,x), x)) x_3^2}{D_+(p,q,x)^4 D_-(p,q,x)^4 |B(p,q,x)|} \right|$$

is continuous and attains its positive minimum on M:

$$N_{V_\delta(\eta),r} := \min_{(p,q,x) \in M} G(p,q,x) > 0.$$

Thus,

$$|\sigma(F^*\psi F)(x, \xi)| = |\sigma(F^*\psi F)(p, q, x, \xi_3)| \ge N_{V_\delta(\eta),r} \frac{1}{\xi_3^2}$$

and accordingly

$$|\sigma(\Lambda)(x, \xi)| = |\sigma(-\Delta \partial_3 F^*\psi F)(x, \xi)| \ge N_{V_{\delta(\eta)},r} |\xi|$$

for $x \in \overline{B_r(y)}$ and $\xi \in V_\delta(\eta) \backslash \{0\}$. Finally,

$$|\sigma(\Lambda)(x, \xi)| \ge \frac{1}{2} N_{V_\delta(\eta),r} (1 + |\xi|) = C_{\delta,\eta,r}(1 + |\xi|)$$

with $C_{\delta,\eta,r} := \frac{1}{2} N_{V_\delta(\eta),r}$ for $x \in B_r(y)$ and $\xi \in V_\delta(\eta)$ with $|\xi| \ge 1$. Hence, Λ is microlocally elliptic of order 1 at (y, η).

The second statement can be validated using Remark 3.3 of [20]. $\qquad\square$

3.4. **Modification of the reconstruction operator.** Recall that we identify both Λ and Λ_δ. The following two results are immediate corollaries of Theorem 3.8.

Corollary 3.10. *For zero offset, $\alpha = 0$, we have that*

$$\sigma(\Lambda)(x, \xi) = \frac{16\pi^5 \xi_3 |\xi_3| \psi\left(x_1 - \frac{\xi_1}{\xi_3} x_3, x_2 - \frac{\xi_2}{\xi_3} x_3, 2|\xi| \frac{x_3}{\xi_3}\right)}{x_3^2 |\xi|}$$

for $x \in \mathbb{R}_+^3$ and $\xi \in \mathbb{R}^3 \backslash \{0\}$ with $\xi_3 \ne 0$. Further, $\sigma(\Lambda)(x, \xi) = 0$ for $x \in \mathbb{R}_+^3$ and $\xi \in \mathbb{R}^3 \backslash \{0\}$ with $\xi_3 = 0$.

Proof. This follows straightforwardly by evaluating the right hand side of (3.6) for $\alpha = 0$. $\qquad\square$

Corollary 3.11. *Let $(x, \xi) \in \mathbb{R}_+^3 \times \mathbb{R}^3$ with $\xi_3 \ne 0$. Then,*

$$\sigma(\Lambda)(x, \xi) \sim \frac{1}{\alpha^2} \ \text{ for } \xi_2 \ne 0 \quad \text{and} \quad \sigma(\Lambda)(x, \xi) \sim \frac{1}{\alpha} \ \text{ for } \xi_2 = 0$$

where "$\sim$" denotes asymptotic equality for $\alpha \to \infty$.

Proof. First, we start with $\xi_2 \neq 0$. We separately consider the two cases that ξ_2 and ξ_3 have the same and opposite signs. For each case we obtain limits of ω, B and αA as $\alpha \to \infty$. From this we can deduce that $\alpha^2 \sigma(\Lambda)(x, \xi)$ has a limit as well for $\alpha \to \infty$. The necessary calculations are lengthy and tedious; see [10, Cor. 3.29] for full details.

If $\xi_2 = 0$, then a direct calculation yields

$$\sigma(\Lambda)(x, \xi) = \frac{16\pi^5 |\xi| \psi\left(x_1 - \frac{\xi_1}{\xi_3}, x_2, \varphi\left(x_1 - \frac{\xi_1}{\xi_3}, x_2, x\right)\right)}{x_3^2 \xi_3 \sqrt{\frac{\alpha^2}{x_3^2} + \frac{\xi_1^2}{\xi_3^2} + 1}\left(\frac{\xi_1^2}{\xi_3^2} + 1\right)},$$

which behaves like $1/\alpha$. $\qquad\square$

Hence, the ellipticity of Λ deteriorates for large α^2/x_3 and and for large x_3/α.

Based on the observations of the last two corollaries, we modify Λ introducing

$$(3.9) \qquad\qquad \Lambda_{\mathrm{mod},0} := -\Delta \partial_3 M F^* \psi F,$$

$$(3.10) \qquad\qquad \Lambda_{\mathrm{mod},i} := -\Delta \partial_3 (M + \alpha^i \, \mathrm{Id}) F^* \psi F \quad \text{for } i \in \{1, 2\}.$$

where M is the multiplication operator by x_3^2. Their top order symbols are

$$\sigma(\Lambda_{\mathrm{mod},0})(x, \xi) = x_3^2 \sigma(\Lambda)(x, \xi), \quad \sigma(\Lambda_{\mathrm{mod},i})(x, \xi) = (x_3^2 + \alpha^i)\sigma(\Lambda)(x, \xi) \quad \text{for } i \in \{1, 2\}.$$

The microlocal ellipticity of the latter two remains unaffected to some extent for large α^2/x_3 and large x_3/α. Furthermore, Proposition 3.9 holds unchanged for the three new operators.

4. Approximate inverse and reconstruction kernels

Our numerical algorithm to compute Λn from the data y given in (2.5) is based on the regularization scheme of approximate inverse [16] because the structure of Λ and its modifications fits perfectly. Instead of Λn we will recover a smoothed version $\Lambda n \star e$ where e is a mollifier, that is, a smooth approximation of the Dirac distribution.

We work with the following family of mollifiers [11]: For $p \in \mathbb{R}_+^3$ and $\gamma, k > 0$ let

$$e_{p,\gamma,k}(x) = C_{\gamma,k} \begin{cases} (\gamma^2 - |x - p|^2)^k, & |x - p| < \gamma, \\ 0, & |x - p| \geq \gamma, \end{cases} \quad x \in \mathbb{R}_+^3,$$

with the normalization constant

$$C_{\gamma,k} = \left(\int_{B_\gamma(p)} (\gamma^2 - |x - p|^2)^k \, \mathrm{d}x\right) = \frac{\Gamma(k + 5/2)}{\pi^{3/2} \varepsilon^{2k+3} \Gamma(k+1)}.$$

The region of integration is $B_\gamma(p)$, the ball of radius γ about p. We have $\mathrm{supp}\, e_{p,\gamma,k} = \overline{B_\gamma(p)}$ and $\int_{\mathbb{R}^3} e_{p,\gamma,k}(x) \, \mathrm{d}x = 1$. Thus, $e_{p,\gamma,k} \to \delta(\cdot - p)$ for $\gamma \to 0$. Here, the parameter γ is a scaling/regularization parameter and k determines the smoothness of $e_{p,\gamma,k}$.

We approximate Λn at p for $n \in \mathcal{E}'(\mathbb{R}_+^3)$ now by

$$(4.1) \qquad L_\gamma n(p) := \langle \Lambda n, e_{p,\gamma,k} \rangle = \langle -\Delta \partial_3 F^* \psi F n, e_{p,\gamma,k} \rangle = \langle \psi F n, F \partial_3 \Delta e_{p,\gamma,k} \rangle$$

where $\langle \cdot, \cdot \rangle$ denotes the usual extension of the L^2 inner product.

Next, we replace Fn by the data y stated in (2.5) and obtain

$$L_\gamma n(p) = \langle \psi y, r_{p,\gamma,k} \rangle = \int_{S_0 \times (2\alpha, \infty)} \psi(s,t) y(s,t) \, r_{p,\gamma,k}(s,t) \, \mathrm{d}(s,t)$$

with the reconstruction kernel

$$r_{p,\gamma,k} := F\partial_3\Delta e_{p,\gamma,k},$$

which is independent of the data and needs to be pre-computed. In what follows, let m_3 be the monomial function $m_3(x) = x_3$ for $x \in \mathbb{R}^3$.

Lemma 4.1. *Let $\gamma > 0$ and $k \geq 3$. With $\widetilde{e}_{p,\gamma,k} = e_{p,\gamma,k}/C_{\gamma,k}$ we have*

$$r_{p,\gamma,k}(s,t) = 4k(k-1)C_{\gamma,k}\Big(5F\big(m_3(\cdot - p)\,\widetilde{e}_{p,\gamma,k-2}\big)$$
$$- 2(k-2)F\big(m_3(\cdot - p)\,|\cdot - p|^2\,\widetilde{e}_{p,\gamma,k-3}\big)\Big)(s,t)$$

for $(s,t) \in S_0 \times (2\alpha, \infty)$.

Proof. A straightforward calculation yields first

$$\Delta\widetilde{e}_{p,\gamma,k}(x) = -6k(\gamma^2 - |x-p|^2)^{k-1} + 4k(k-1)|x-p|^2(\gamma^2 - |x-p|^2)^{k-2}\chi_{B_\gamma(p)}(x)$$

and then

$$\partial_3\Delta\widetilde{e}_{p,\gamma,k}(x) = \Big(20k(k-1)(x_3 - p_3)(\gamma^2 - |x-p|^2)^{k-2}$$
$$- 8k(k-1)(k-2)(x_3 - p_3)|x-p|^2(\gamma^2 - |x-p|^2)^{k-3}\Big)\chi_{B_\gamma(p)}(x).$$

The assertion follows from $e_{p,\gamma,k} = C_{\gamma,k}\widetilde{e}_{p,\gamma,k}$. $\qquad\qquad\square$

Analogously, we define the approximations

$$(4.2) \qquad L_{\gamma,\mathrm{mod},i}n(p) := \langle\Lambda_{\mathrm{mod},i}n, e_{p,\gamma,k}\rangle = \langle\psi Fn, r_{p,\gamma,k,\mathrm{mod},i}\rangle \quad \text{for } i \in \{0,1,2\}$$

with the corresponding kernels

$$r_{p,\gamma,k,\mathrm{mod},0} := FM\partial_3\Delta e_{p,\gamma,k} \quad \text{and} \quad r_{p,\gamma,k,\mathrm{mod},i} := F(M + \alpha^i\,\mathrm{Id})\partial_3\Delta e_{p,\gamma,k}, \ i \in \{1,2\}.$$

Corollary 4.2. *Let $\gamma > 0$, $k \geq 3$, and $\widetilde{e}_{p,\gamma,k}$ be as in Lemma 4.1. Then, for $(s,t) \in S_0 \times (2\alpha, \infty)$,*

$$r_{p,\gamma,k,\mathrm{mod},0}(s,t) = 4k(k-1)C_{\gamma,k}\Big(5F\big(m_3(\cdot - p)\,m_3^2\,\widetilde{e}_{p,\gamma,k-2}\big)$$
$$- 2(k-2)F\big(m_3(\cdot - p)\,m_3^2\,|\cdot - p|^2\,\widetilde{e}_{p,\gamma,k-3}\big)\Big)(s,t)$$

and

$$r_{p,\gamma,k,\mathrm{mod},i}(s,t) = r_{p,\gamma,k,\mathrm{mod},0}(s,t) + \alpha^i\,r_{p,\gamma,k}(s,t), \ i \in \{1,2\}.$$

4.1. The elliptic Radon transform of a characteristic function supported in a ball. For the computation of the reconstruction kernels according to the above lemma and corollary we have to apply F to functions which are supported in a ball $B_r(P)$ for $P = (p_1, p_2, p_3) \in \mathbb{R}_+^3$ and $0 < r < p_3$. Let $n \in L^2(\mathbb{R}_+^3)$ with $\mathrm{supp}(n) \subseteq B_r(P)$. Using the ellipsoids of the Radon transform, this situation is illustrated in Figure 1, where n vanishes outside the ball $B_r(P)$. To calculate Fn, we first shift the coordinate system (x_1, x_2, x_3) such that $(s_1, s_2, 0)^\top$ is the new origin. Afterwards, we rotate the system
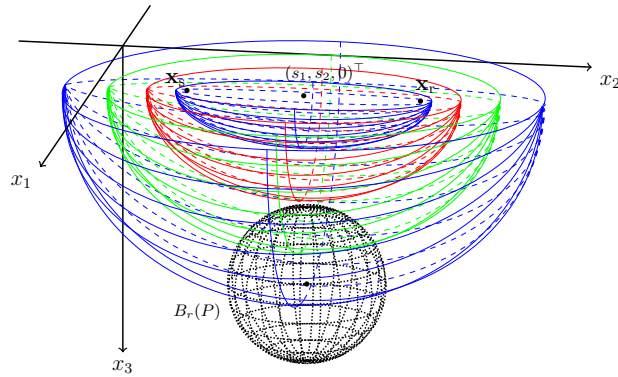
FIGURE 1. The given situation for several travel times t, respectively. Each travel time t is associated with one open half ellipsoid for fixed $s \in S_0$.
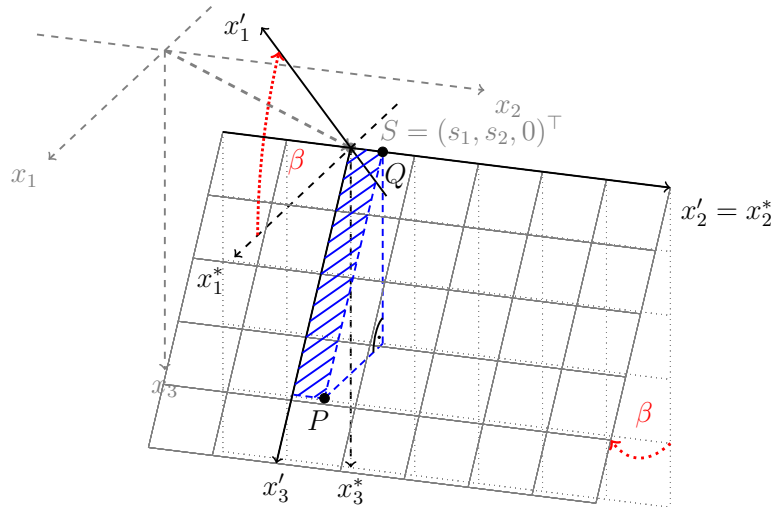

FIGURE 2. The shift into the coordinate system (x_1^*, x_2^*, x_3^*) and afterwards, the rotation into the new coordinate system (x_1', x_2', x_3') such that $(s_1, s_2, 0)^\top$ is the origin and P lies in the x_2'-x_3'-plane. Here, the point Q is given by $(0, p_2', 0)^\top$.

in such a way that P lies in the $x_2' - x_3'$-plane in the coordinate system (x_1', x_2', x_3'). This rotation R is given by the following matrix

$$R = \begin{pmatrix} \cos(\beta) & 0 & -\sin(\beta) \\ 0 & 1 & 0 \\ \sin(\beta) & 0 & \cos(\beta) \end{pmatrix}, \quad \beta = \arctan((p_1 - s_1)/p_3).$$

Using the notation $\mathbf{s} := (s, 0)^\top = (s_1, s_2, 0)^\top$, we calculate

$$Fn(s, t) = \int_{\mathbb{R}^3_+} n(x) A(s, x) \delta(t - \varphi(s, x)) \, \mathrm{d}x = \int_{\mathbb{R}^3} n(x) A(s, x) \chi_{B_r(P)}(x) \delta(t - \varphi(s, x)) \, \mathrm{d}x$$

$$= \int_{\mathbb{R}^3} n(R^{-1}x + \mathbf{s}) A((0,0), x) \chi_{B_r(P')}(x) \delta(t - \varphi((0,0), x)) \, \mathrm{d}x$$

where

$$P' = (0, p'_2, p'_3) = R(P - \mathbf{s}) = \left(0, p_2 - s_2, \frac{p_3}{\cos\left(\arctan\left(\frac{p_1 - s_1}{p_3}\right)\right)}\right)^\top.$$

The last component p'_3 of P' is calculated with the help of two trigonometric relations in a suitable right triangle in the $x'_2 = p'_2$-plane, see Figure 2. Next, we introduce the prolate spheroidal coordinates in $\mathbb{R}^3$, which are realized by $x = x(s, t, \phi, \theta)$ with components

$$x_1 = s_1 + \sqrt{\tfrac{1}{4}t^2 - \alpha^2} \sin(\phi) \cos(\theta),$$

(4.3)
$$x_2 = s_2 + \tfrac{1}{2} t \cos(\phi),$$

$$x_3 = \sqrt{\tfrac{1}{4}t^2 - \alpha^2} \sin(\phi) \sin(\theta),$$

for $t > 2\alpha$, $\phi \in (0, \pi)$ and $\theta \in (0, 2\pi)$. These coordinates fit to prolate spheroids, i.e., rotational ellipsoids with two half axes having the same length and a longer third one, which is the rotational axis. Such ellipsoids are just given by $t = \varphi(s, x)$ for $x \in \mathbb{R}^3$. The variable t is the travel time, the angle θ the rotational angle and the foci are $(s_1, s_2 - \alpha, 0)^\top$ and $(s_1, s_2 + \alpha, 0)^\top$. The different angles of θ are arranged concentrically whereas the angles ϕ are located in hyberbolic orbits.

Since we consider the situation in the new coordinate system (x'_1, x'_2, x'_3), we set $s_1 = s_2 = 0$ and so the ellipsoids we consider have the two foci $(0, -\alpha, 0)^\top$ and $(0, \alpha, 0)^\top$. Hence, we write $x = x(0, t, \phi, \theta) = x(t, \phi, \theta)$ and obtain

(4.4) $$Fn(s, t) = \frac{1}{2} \int_{\theta_{\min}}^{\theta_{\max}} \int_{\phi(\theta)_{\min}}^{\phi(\theta)_{\max}} n(R^{-1}x(t, \phi, \theta) + \mathbf{s}) \chi_{B_r(P')}(x(t, \phi, \theta)) \sin(\phi) \, \mathrm{d}\phi \, \mathrm{d}\theta$$

where $\theta_{\min}$ and $\theta_{\max}$ are defined by

$$\theta_{\min / \max} = \theta_{\min / \max}(t) := \min / \max\{\theta \in [0, 2\pi) \,|\, x(t, \phi, \theta) \in \overline{B_r(P')},\ \phi \in [0, \pi)\}$$

for fixed $t \in (2\alpha, \infty)$. Further, $\phi(\theta)_{\min}$ and $\phi(\theta)_{\max}$ are given by

$$\phi(\theta)_{\min / \max} = \phi(\theta, t)_{\min / \max} := \min / \max\{\phi \in [0, \pi) \,|\, x(t, \phi, \theta) \in \overline{B_r(P')}\}$$

for fixed $\theta \in (\theta_{\min}, \theta_{\max})$ and $t \in (2\alpha, \infty)$.

Before we go into further details regarding these four angles, we limit the interval $(2\alpha, \infty)$ of the travel time t. In the new coordinate system the considered ellipsoids have the two foci $(0, -\alpha, 0)^\top$ and $(0, \alpha, 0)^\top$. As in the original situation illustrated in Figure 1, these ellipsoids intersect $B_r(P)$ only for travel times t in a bounded interval. The minimal and maximal values are

$$T_{\min} := \min_{y \in C}(|(0, -\alpha, 0)^\top - y| + |y - (0, \alpha, 0)^\top|)$$

and

$$T_{\max} := \max_{y \in C}(|(0, -\alpha, 0)^\top - y| + |y - (0, \alpha, 0)^\top|)$$

where C is the circle which is the intersection of the $x_2' - x_3'$-plane with the boundary of the ball $B_r(P')$. So, we have $Fn(s,t) = 0$ for $s \in S_0$ and $t \leq T_{\min}$ or $t \geq T_{\max}$. All further details can be found in [10, Sec. 4.2.4].

Now, we sketch how to obtain the four angles limiting the integrals. In case of $\theta_{\min}$ and $\theta_{\max}$ we consider the plane $x_2 = p_2'$. We are thus in a two dimensional setting, in which $\theta_{\min}$ and $\theta_{\max}$ are the two angles of θ in prolate spheroidal coordinates enclosing the associated cross section of the ball $B_r(P')$. An illustration is given in the left image of Figure 3. For the calculation of $\theta_{\min}$ and $\theta_{\max}$ we determine the angle $\vartheta_{\max}$ marked in Figure 3 and use the symmetry with respect to $\theta = \pi/2$, see [10, Sec. 4.2.3] for exhaustive explanations.
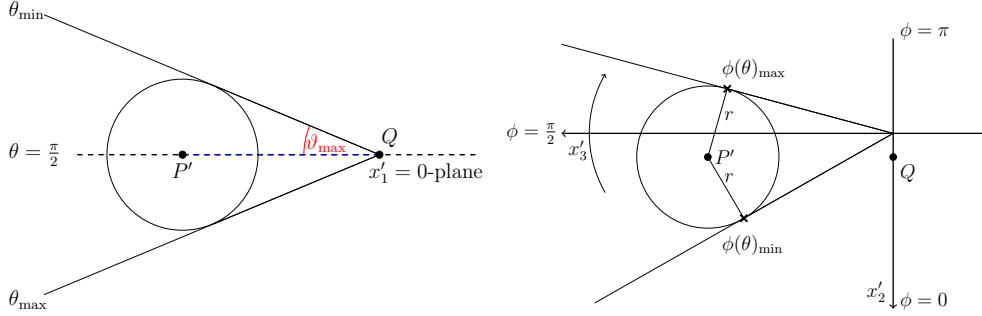
FIGURE 3. Left: An illustration of $\theta_{\min}$ and $\theta_{\max}$ in the $x_2' = p_2'$-plane. Right: The angles $\phi(\theta)_{\min}$ and $\phi(\theta)_{\max}$ marked in the $x_1' = 0$-plane from a bird's eye view.

To get $\phi(\theta)_{\min}$ and $\phi(\theta)_{\max}$, we fix $\theta \in [\theta_{\min}, \theta_{\max}]$. The angles $\phi(\theta)_{\min}$ and $\phi(\theta)_{\max}$ are given by the minimal and maximal angles of ϕ corresponding to the points on $\partial B_r(P')$ for fixed $\theta \in (\theta_{\min}, \theta_{\max})$ as illustrated in the right image of Figure 3. Thus, we have to solve the equation

$$r^2 = |P' - x(t, \phi(\theta), \theta)|^2$$

for $\phi(\theta)$ in our new coordinate system (x_1', x_2', x_3'). By the definition of the prolate spheroidal coordinates this equation has exactly two solutions $\phi(\theta)$ in $[0, \pi)$. Next, we insert these coordinates setting $s_1 = s_2 = 0$ in (4.3) and get, using the substitution $z = \cos(\phi(\theta))$, the following identity

$$r^2 = (p_2')^2 + (p_3')^2 + \tfrac{1}{4}t^2 - \alpha^2(1 - z^2) - p_2'tz - p_3'\sqrt{t^2 - 4\alpha^2}\sqrt{1 - z^2}\sin(\theta).$$

Solving this equation and resubstitution yield two solutions z_1 and z_2 in $[-1, 1]$. Without loss of generality, we obtain

$$\phi(\theta)_{\min} = \arccos(z_1) \quad \text{and} \quad \phi(\theta)_{\max} = \arccos(z_2)$$

with $\phi(\theta)_{\min} < \phi(\theta)_{\max}$. In our implementation we obtain z_1 and z_2 approximately by Newton's method.
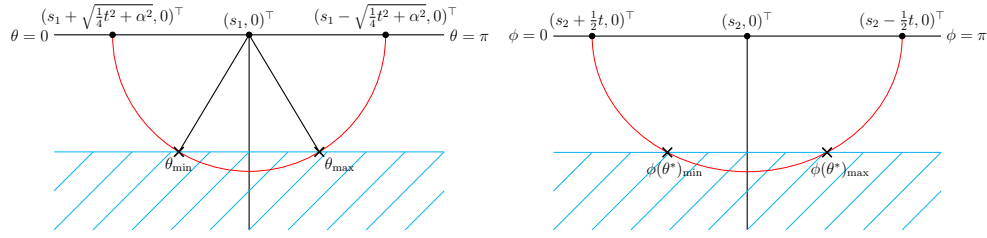
FIGURE 4. Left: The minimal and maximal possible angle for θ illustrated in the $x_2 = s_2$-plane. Right: In the $\theta = \theta^*$-plane we consider the angles $\phi(\theta^*)_{\min}$ and $\phi(\theta^*)_{\max}$, which are determined by the coordinates of the two marked points.

4.2. **The elliptic Radon transform of the characteristic function of a half space.** For our numerical experiments in the next section we provide Fn where n is the characteristic function of a half space, i.e., $n = \chi_{\{x \in \mathbb{R}^3_+ \mid x_3 \geq l\}}$ for some $l > 0$. We directly work in prolate spheroidal coordinates (4.3), this time with arbitrary s_1, s_2 and restricted to $\mathbb{R}^3_+$, i.e., $t \in (2\alpha, \infty)$, $\phi \in [0, \pi)$, and $\theta \in [0, \pi)$. Hence, by $x = x(s, t, \phi, \theta)$,

$$Fn(s, t) = \frac{1}{2} \int_{\theta_{\min}}^{\theta_{\max}} \int_{\phi(\theta)_{\min}}^{\phi(\theta)_{\max}} n(x(s, t, \phi, \theta)) \sin(\phi) \, d\phi \, d\theta$$

for $(s, t) \in S_0 \times (2\alpha, \infty)$ with

$$\theta_{\min / \max} = \theta_{\min / \max}(s, t) := \min / \max\{\theta \in [0, \pi) \mid x(s, t, \phi, \theta) \in \mathrm{supp}(n), \phi \in [0, \pi)\}$$

and

$$\phi(\theta)_{\min / \max} := \phi(\theta)_{\min / \max}(s, t) := \min / \max\{\phi \in [0, \pi) \mid x(s, t, \phi, \theta) \in \mathrm{supp}(n)\}.$$

We have $n(x(s, t, \phi, \theta)) = 1$ for $\theta \in (\theta_{\min}, \theta_{\max})$ and $\phi(\theta) \in (\phi(\theta)_{\min}, \phi(\theta)_{\max})$. Otherwise, $n(x(s, t, \phi, \theta)) = 0$. Therefore,

$$(4.5) \qquad Fn(s, t) = \frac{1}{2} \int_{\theta_{\min}}^{\theta_{\max}} \int_{\phi(\theta)_{\min}}^{\phi(\theta)_{\max}} \sin(\phi) \, d\phi \, d\theta, \quad (s, t) \in S_0 \times (2\alpha, \infty).$$

We obtain the four required angles from the points of intersection marked with a cross in Figure 4. For $\theta_{\min}$ and $\theta_{\max}$ we consider the plane $x_2 = s_2$ where $\phi = \pi/2$ according to (4.3). As $x_3 = l$ for the points in Figure 4, we need to solve $l = x_3 = \sqrt{\frac{1}{4}t^2 - \alpha^2} \sin(\theta)$ for θ yielding

$$\theta_{\min} = \arcsin\left(\frac{l}{\sqrt{\frac{1}{4}t^2 - \alpha^2}}\right) \quad \text{and} \quad \theta_{\max} = \pi - \theta_{\min}.$$

A similar reasoning leads to $\phi(\theta)_{\min}$ and $\phi(\theta)_{\max}$ for $\theta^* \in [\theta_{\min}, \theta_{\max}]$. We consider the plane $\theta = \theta^*$ illustrated in the right image of Figure 4. Here, the equation is $l = \sqrt{\frac{1}{4}t^2 - \alpha^2} \sin(\phi(\theta^*)) \sin(\theta^*)$, which is solved by

$$\phi(\theta^*)_{\min} = \arcsin\left(\frac{l}{\sqrt{\frac{1}{4}t^2 - \alpha^2} \sin(\theta^*)}\right) \quad \text{and} \quad \phi(\theta^*)_{\max} = \pi - \phi(\theta^*)_{\min}.$$

If the travel time t is too small, then the ellipsoids do not intersect the half space. The limiting travel time is given by $T_{\min} = \min_{\{x \in \mathbb{R}^3_+ \mid \varphi(s,x)=t\}}(|\mathbf{x}_s(s) - x| + |x - \mathbf{x}_r(s)|)$. Obviously, the minimum is attained at $x = (s_1, s_2, l)$ with minimal value $T_{\min} = 2\sqrt{\alpha^2 + l^2}$. Thus, $Fn(s,t) = 0$ for $t \leq T_{\min}$ and $s \in S_0$.

4.3. Computation of the reconstruction kernels.

By the representation of $r_{p,\gamma,3}$ in Lemma 4.1 and the results of Section 4.1 we have

$$r_{p,\gamma,3}(s,t)$$
$$= C_{\gamma,3}\frac{1}{2}\int_{\theta_{\min}}^{\theta_{\max}}\int_{\phi(\theta)_{\min}}^{\phi(\theta)_{\max}}\left(120\gamma^2\Big([R^{-1}x(t,\phi,\theta) + (s_1,s_2,0)^\top]_3 - p_3\Big)\right.$$
$$\left.- 168\Big([R^{-1}x(t,\phi,\theta) + (s_1,s_2,0)^\top]_3 - p_3\Big)|R^{-1}x(t,\phi,\theta) + (s_1,s_2,0)^\top - p|^2\right)$$
$$\chi_{B_\gamma(p')}(x(t,\phi,\theta))\sin(\phi)\,\mathrm{d}\phi\,\mathrm{d}\theta$$

$$= \frac{315}{64\pi\gamma^9}\frac{1}{2}\int_{\theta_{\min}}^{\theta_{\max}}\int_{\phi(\theta)_{\min}}^{\phi(\theta)_{\max}}\left(120\gamma^2(-\sin(\beta)\cos(\theta) + \cos(\beta)\sin(\theta))\sqrt{\tfrac{1}{4}t^2 - \alpha^2}\sin^2(\phi)\right.$$
$$- 120\gamma^2 p_3\sin(\phi)$$
$$- 168(-\sin(\beta)\cos(\theta) + \cos(\beta)\sin(\theta))\sqrt{\tfrac{1}{4}t^2 - \alpha^2}|x(t,\phi,\theta) - p'|^2\sin^2(\phi)$$
$$\left.+ 168p_3|x(t,\phi,\theta) - p'|^2\sin(\phi)\right)\chi_{B_\gamma(p')}(x(t,\phi,\theta))\,\mathrm{d}\phi\,\mathrm{d}\theta$$

for $(s,t) \in S_0 \times (T_{\min}, T_{\max})$. Further,

$$(4.6) \qquad |x(t,\phi,\theta) - p'|^2 = (a + b\sin(\phi))^2 + (c + d\cos(\phi))^2 + (e + f\sin(\phi))^2$$

where

$$a = -p'_1 = 0, \qquad b = \sqrt{\tfrac{1}{4}t^2 - \alpha^2}\cos(\theta), \qquad\qquad c = -p'_2 = -p_2 + s_2,$$
$$d = \tfrac{1}{2}t, \qquad e = -p'_3 = -\frac{p_3}{\cos\left(\arctan\left(\frac{p_1 - s_1}{p_3}\right)\right)}, \qquad f = \sqrt{\tfrac{1}{4}t^2 - \alpha^2}\sin(\theta),$$

for $t \in (T_{\min}, T_{\max})$, $\phi \in [0, \pi)$ and $\theta \in [0, 2\pi)$. Hence, to compute numerical values for $r_{p,\gamma,3}$, we need the antiderivates of the following functions

$$\phi \mapsto \sin^2(\phi), \qquad \phi \mapsto (a + b\sin(\phi))^2 + (c + d\cos(\phi))^2 + (e + f\sin(\phi))^2\sin^2(\phi),$$
$$\phi \mapsto \sin(\phi), \qquad \phi \mapsto (a + b\sin(\phi))^2 + (c + d\cos(\phi))^2 + (e + f\sin(\phi))^2\sin(\phi).$$

As these four functions are trigonometric polynomials in ϕ, their antiderivates exist in closed form. We found analytic expressions by a computer algebra system and imported them in our code.

Analogously,

$$r_{p,\gamma,3,\mathrm{mod},0}(s,t)$$

$$= \frac{315}{64\pi\gamma^9} \frac{1}{2} \int_{\theta_{\min}}^{\theta_{\max}} \int_{\phi(\theta)_{\min}}^{\phi(\theta)_{\max}} \left(120\gamma^2(-\sin(\beta)\cos(\theta) + \cos(\beta)\sin(\theta))^3 \right.$$

$$\times \left(\sqrt{\tfrac{1}{4}t^2 - \alpha^2} \right)^3 \sin^4(\phi)$$

$$- 120\gamma^2 p_3(-\sin(\beta)\cos(\theta) + \cos(\beta)\sin(\theta))^2 \left(\sqrt{\tfrac{1}{4}t^2 - \alpha^2} \right)^2 \sin^3(\phi)$$

$$- 168(-\sin(\beta)\cos(\theta) + \cos(\beta)\sin(\theta))^3 \left(\sqrt{\tfrac{1}{4}t^2 - \alpha^2} \right)^3 |x(t,\phi,\theta) - p'|^2 \sin^4(\phi)$$

$$+ 168 p_3(-\sin(\beta)\cos(\theta) + \cos(\beta)\sin(\theta))^2 \left(\sqrt{\tfrac{1}{4}t^2 - \alpha^2} \right)^2 |x(t,\phi,\theta) - p'|^2 \sin^3(\phi) \right)$$

$$\chi_{B_\gamma(p')}(x(t,\phi,\theta))\,\mathrm{d}\phi\,\mathrm{d}\theta.$$

In view of (4.6) we now need the antiderivatives of

$$\phi \mapsto \sin^4(\phi), \qquad \phi \mapsto (a + b\sin(\phi))^2 + (c + d\cos(\phi))^2 + (e + f\sin(\phi))^2 \sin^4(\phi),$$

$$\phi \mapsto \sin^3(\phi), \qquad \phi \mapsto (a + b\sin(\phi))^2 + (c + d\cos(\phi))^2 + (e + f\sin(\phi))^2 \sin^3(\phi),$$

which we obtain analytically as before.

Knowing $r_{p,\gamma,3}$ and $r_{p,\gamma,3,\mathrm{mod},0}$ means knowing $r_{p,\gamma,k,\mathrm{mod},1}$ and $r_{p,\gamma,k,\mathrm{mod},2}$ as well due to Corollary 4.2. All in all, we have the explicit expressions of the different reconstruction kernels at a point $(s,t) \in S_0 \times (2\alpha,\infty)$ depending on the limiting angles $\theta_{\min}$, $\theta_{\max}$, $\phi_{\min}(\theta)$ and $\phi_{\max}(\theta)$ and the travel times $T_{\min}$ and $T_{\max}$.

5. Numerical experiments

For the numerical examples we have to evaluate integrals of the from

$$\widetilde{L}_\gamma n(p) = \langle \psi y, \widetilde{r}_{p,\gamma,3} \rangle = \int_{S_0 \times (2\alpha,\infty)} \psi(s,t) y(s,t) \widetilde{r}_{p,\gamma,3}(s,t)\,\mathrm{d}(s,t)$$

for $p \in \mathbb{R}_+^3$ where y is the given data and $\widetilde{r}_{p,\gamma,3}$ represents one of the kernels belonging to the four imaging operators Λ, $\Lambda_{\mathrm{mod},i}$, $i \in \{0,1,2\}$. Further, the cutoff function $\psi \in C_c^\infty(S_0 \times (2\alpha,\infty))$ is taken from [20, Sec. 5]: For $\overline{S} > 0$ and $\overline{T} > \underline{T} > 0$ we set

$$(5.1) \qquad \psi(s,t) = \psi(s_1,s_2,t) = \Psi_1(s_1)\Psi_1(s_2)\Psi_2(t),$$

where

$$\Psi_1(s) = \begin{cases} 1, & \text{for} & |s| < \overline{S}, \\ h(|s|,\overline{S}), & \text{for} & \overline{S} \le |s| \le \overline{S} + 1, \\ 0, & \text{for} & \overline{S} + 1 < |s|, \end{cases}$$

and

$$\Psi_2(t) = \begin{cases} 0, & \text{for} & t \le \underline{T}, \\ g(t,\underline{T}), & \text{for} & \underline{T} < t < 2\underline{T}, \\ 1, & \text{for} & 2\underline{T} \le t \le \overline{T}, \\ h(t,\overline{T}), & \text{for} & \overline{T} < t < \overline{T} + 1, \\ 0, & \text{for} & \overline{T} + 1 \le t. \end{cases}$$

The functions f, g, and h are defined as follows

$$f(r) = \begin{cases} \exp(-\frac{1}{r}), & \text{for} \quad 0 < r, \\ 0, & \text{for} \quad r \leq 0, \end{cases}$$

$$g(t, \underline{T}) = \frac{f(\frac{t}{\underline{T}} - 1)}{f(\frac{t}{\underline{T}} - 1) + f(2 - \frac{t}{\underline{T}})}, \qquad h(t, \overline{T}) = \frac{f(\overline{T} + 1 - t)}{f(\overline{T} + 1 - t) + f(t - \overline{T} - \frac{1}{2})}.$$

Then,

$$\text{supp}(\psi) \subseteq [-\overline{S} - 1, \overline{S} + 1] \times [\underline{T}, \overline{T} + 1] \quad \text{and} \quad \psi_{\big|_{[-\overline{S}, \overline{S}] \times [2\underline{T}, \overline{T}]}} = 1.$$

In our numerical experiments we assume to know the data y at the uniformly distributed values $(s_1^{(i)}, s_2^{(j)}, t^{(k)}) \in [-s_{\max}, s_{\max}]^2 \times [t_{\min}, t_{\max}]$, $i, j \in \{1, \dots N_s\}$, $k \in \{1, \dots, N_t\}$, where $s_{\max} > 0$, $t_{\max} > t_{\min} > 2\alpha$, and $N_s, N_t \in \mathbb{N}$. The respective step sizes are $h_s = 2s_{\max}/N_s$ and $h_t = (t_{\max} - t_{\min})/N_t$.

Since the kernel vanishes for travel times below $T_{\min} = T_{\min}(s_1^{(i)}, s_2^{(j)}, \gamma, p)$ and above $T_{\max} = T_{\max}(s_1^{(i)}, s_2^{(j)}, \gamma, p)$, see Section 4.1, we can restrict the $t^{(k)}$'s to the interval

$$\mathcal{T}_{i,j}(\gamma, p) := \left(T_{\min}(s_1^{(i)}, s_2^{(j)}, \gamma), T_{\max}(s_1^{(i)}, s_2^{(j)}, \gamma) \right).$$

Thus, we approximate $\widetilde{L}_\gamma$ straightforwardly by the quadrature rule

$$(5.2) \quad \mathrm{Q}\,\widetilde{L}_\gamma n(p) := h_t h_s^2 \sum_{i,j=1}^{N_s} \sum_{t^{(k)} \in \mathcal{T}_{i,j}(\gamma, p)} \psi(s_1^{(i)}, s_2^{(j)}, t^{(k)}) y(s_1^{(i)}, s_2^{(j)}, t^{(k)}) \\ \times \widetilde{r}_{p, \gamma, 3}(s_1^{(i)}, s_2^{(j)}, t^{(k)}).$$

In order not to overload the notation, we refrain from specifying all parameters on which Q depends. Below we will write $\mathrm{Q}\,L_\gamma$ and $\mathrm{Q}\,L_{\gamma, \text{mod}, i}$, $i \in \{0, 1, 2\}$, to indicate which operator (kernel) is actually used in (5.2), compare (4.1) and (4.2).

5.1. **Reconstructions from consistent data.** For the first set of numerical experiments we choose the function n to be reconstructed as

$$n = \chi_{B_2(0,0,4)} - \chi_{B_1(0,0,4)} + \chi_{B_{1.5}(3,0,5)} + \chi_{\{x_3 \geq 6.5\}},$$

see Figure 5. We generate the data y numerically by evaluating Fn as we have demonstrated in the previous section.

First, we discuss which features of n we expect to see in $\widetilde{L}_\gamma n$. This discussion applies to all four instances of $\widetilde{L}_\gamma$ as all underlying imaging operators enjoy the same order and the same decisive microlocal properties. Indeed, let $\widetilde{\Lambda} \in \{\Lambda, \Lambda_{\text{mod}, i} \,|\, i \in \{0, 1, 2\}\}$. Then, $\widetilde{\Lambda}$ is microlocally elliptic of order 1 at $(x_*, \xi_*) \in \mathbb{R}_+^3 \times \mathbb{R}^3 \setminus \{0\}$ if

$$\xi_* \in C(x_*) = \{\xi \in \mathbb{R}^3 \,|\, \xi_3 \neq 0, \psi(s(x_*, \xi), \varphi(s(x_*, \xi), x_*)) > 0\},$$

see Proposition 3.9. Hence, by Theorem 3.6,

$$(5.3) \qquad (x_*, \xi_*) \in \text{WF}^{-1/2}(\widetilde{\Lambda} n) \quad \text{for } (x_*, \xi_*) \in \text{WF}(n) = \text{WF}^{1/2}(n).$$

This means: If the third component of the normal ξ_* at an element x_* of the singular support of n does not vanish and if $\psi(x_*) > 0$, then the Sobolev smoothness of $\widetilde{\Lambda} n(x_*)$ drops by one order in direction ξ_*. More precisely, the smoothness decreases from $H^{1/2}$ to $H^{-1/2}$. So, if we choose ψ such that it does not vanish on the support of n, all singularities in the cross section $x_2 = 0$ are emphasized by $\widetilde{\Lambda}$ except for the singularities at the points marked in red in Figure 5.
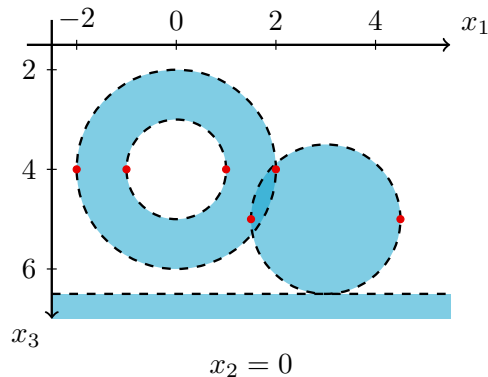
FIGURE 5. Cross section of the function n for $x_2 = 0$. On the darker blue area, where the two large circles overlap, n is equal to 2, on the light blue area to 1 and off the blue areas it is 0. The singularities marked in red get not emphasized since their third component of the normal direction is zero.

Recall that

$$(5.4) \qquad\qquad \mathrm{WF}(\widetilde{\Lambda}n) \subseteq \mathrm{WF}(F^*\psi F n)$$

by the pseudolocal property of Theorem 3.5. Further, $(x, \xi) \in \mathrm{WF}(F^*\psi F n)$ only if there exists $s \in S_0$ and $\omega \neq 0$ such that $\xi = \omega \nabla_x \varphi(s, x)$, see Theorem 3.7. Since the set S_0 is bounded in applications, there will be pairs (x, ξ) for which no $s \in S_0$ and $\omega \neq 0$ exist. Those singularities will not be preserved; they are not visible in $\widetilde{\Lambda}n$.

In the sequel, we provide the approximations $Q\,L_\gamma n$, $Q\,L_{\gamma,\mathrm{mod},0}n$, and $Q\,L_{\gamma,\mathrm{mod},2}n$. To be able to compare the results, we consider the same setting with two offsets $\alpha = 1$ and $\alpha = 10$. Further, we choose $t_{\min} = 2\alpha + 0.1$, $t_{\max} = t_{\min} + 17$, $s_{\max} = 10$, and $N_s = N_t = 600$. Thus, the data are integral values of n over $216\,000\,000$ ellipsoids. From this data the reconstruction is evaluated in the cross section $[-2.5, 5] \times \{0\} \times [1.5, 7]$ at uniformly distributed points where $N_{x_1} = 135$ and $N_{x_3} = 99$ values are used for the first and third coordinate, respectively. Finally, we use the trapezoidal rule to numerically compute the integrals with respect to θ in (4.4) and (4.5) and also in the reconstruction kernels (Section 4.3). The numbers of uniformly distributed integration nodes are 201 for (4.4), 16 for (4.5), and 50 for the kernels.

Figure 6 displays the reconstructions with respect to Λ from (3.10). We recover all predicted singularities, i.e., all singularities are imaged except for the ones at the outermost points of the balls. Nevertheless, in case of $\alpha = 1$ singularities closer to the surface are more emphasized than the ones further away. For $\alpha = 10$ we make a different observation: the intensity of the singularities is nearly independent of the distance to the surface.

We defined the first modified reconstruction operator $\Lambda_{\mathrm{mod},0}$ in (3.9) to compensate the behavior of the top order symbol of Λ for small values of α compared to x_3. The
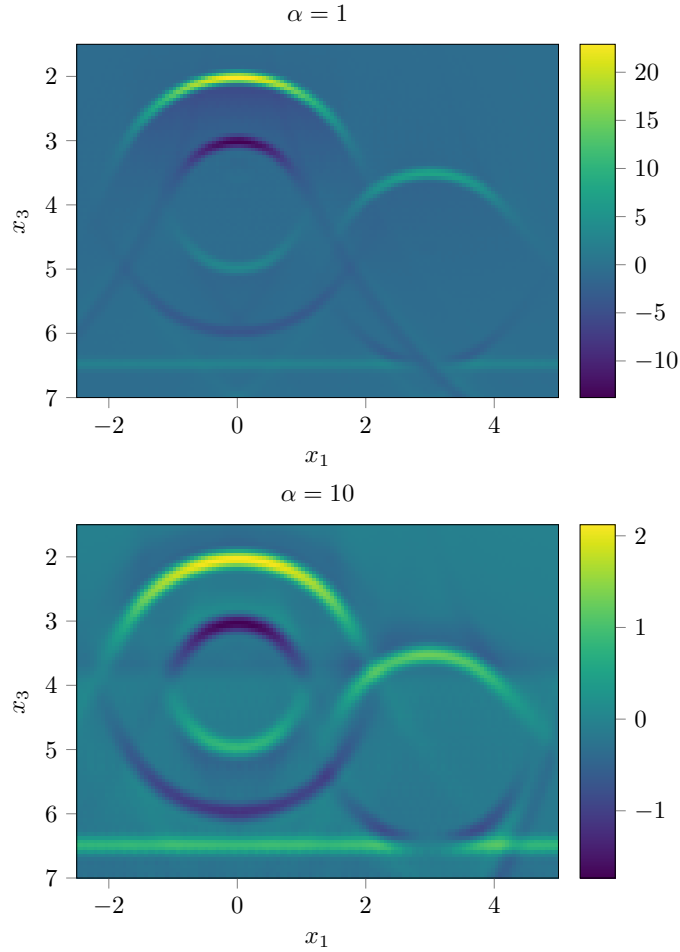
FIGURE 6. Cross sections $Q\,L_\gamma n(\cdot, 0, \cdot)$ for Λ from (3.1). They differ in the offset α and the regularization parameter γ, which depends on the offset. In case of $\alpha = 1$ we have $\gamma = 0.2$, for $\alpha = 10$ it is $\gamma = 0.3$.

results are in Figure 7. In comparison to the reconstructions in Figure 6 the intensity of the singularities for $\alpha = 1$ is significantly more uniform and more independent of their x_3-coordinate. However, in case of $\alpha = 10$ the strength of the reconstructed singularities is less uniform than with Λ. These observations are in complete agreement with our theoretical considerations leading to the definition of $\Lambda_{\mathrm{mod},0}$.

To achieve further improvements in case α is large compared to x_3, we introduced the operators $\Lambda_{\mathrm{mod},1}$ and $\Lambda_{\mathrm{mod},2}$, see (3.10). The approximation $Q\,L_{\gamma,\mathrm{mod},1} n$ differs only slightly from those obtained by using $Q\,L_{\gamma,\mathrm{mod},0} n$; thus, they are not included here; we refer to [10, Fig. 5.18]. Figure 8 displays cross sections of $Q\,L_{\gamma,\mathrm{mod},2} n$. As expected, adding the operator $\alpha^2 \Lambda$ to $\Lambda_{\mathrm{mod},0}$ guarantees that the reconstructed strength of singularities is independent of their depth coordinates, especially for α^2/x_3 large (image on the bottom of Figure 8).
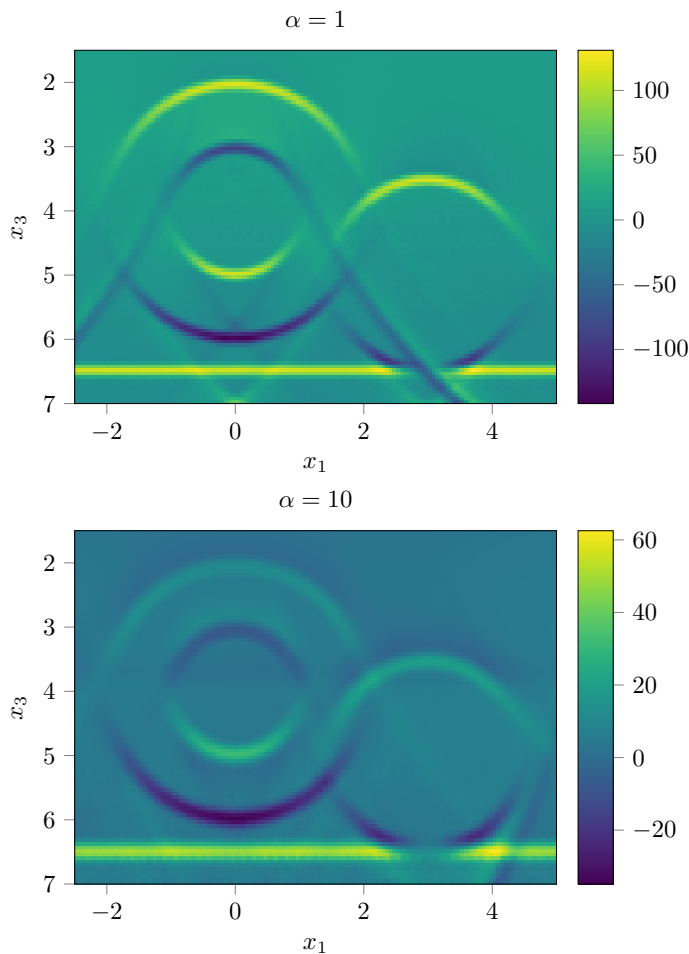
$$\alpha = 1$$

$$\alpha = 10$$

FIGURE 7. Cross sections $\mathrm{Q}\, L_{\gamma,\mathrm{mod},0} n(\cdot, 0, \cdot)$ for $\Lambda_{\mathrm{mod},0}$ from (3.9).
Top: $\alpha = 1$ and $\gamma = 0.2$, bottom: $\alpha = 10$ and $\gamma = 0.3$.

To give you an impression on the 3D nature of our setting, we added two further cross sections with x_2-coordinates different from 0. In Figure 9 you find $\mathrm{Q}\, L_{\gamma,\mathrm{mod},0} n_*$ where $n_* = n - \chi_{\{x_3 \geq 6.5\}}$, that is, n_* only consists of the characteristic functions of the balls. All parameters entering Q are chosen similarly as before.

In each Figure 6-9, we see artifact curves that seem to come tangentially out of the location of the non-visible singularities (red dots in Figure 5). Similar artifacts are explained in [9] for a spherical transform. Although those results are for a different transform, they do suggest that some artifacts in Figures 6-9 could be along integration surfaces $E(s,t)$ for (s,t) in the boundary of the data set and for which the surface $E(s,t)$ is tangent to a boundary of the object. There is a second type of artifact, too, that is not tangent to a boundary of the object. If you compare the top image in Figures 6-8 with the top image of Figure 9 (that does not include a half space starting at $x_3 = 6.5$), you see clearly that there are artifacts that seem to be independent of the disks and
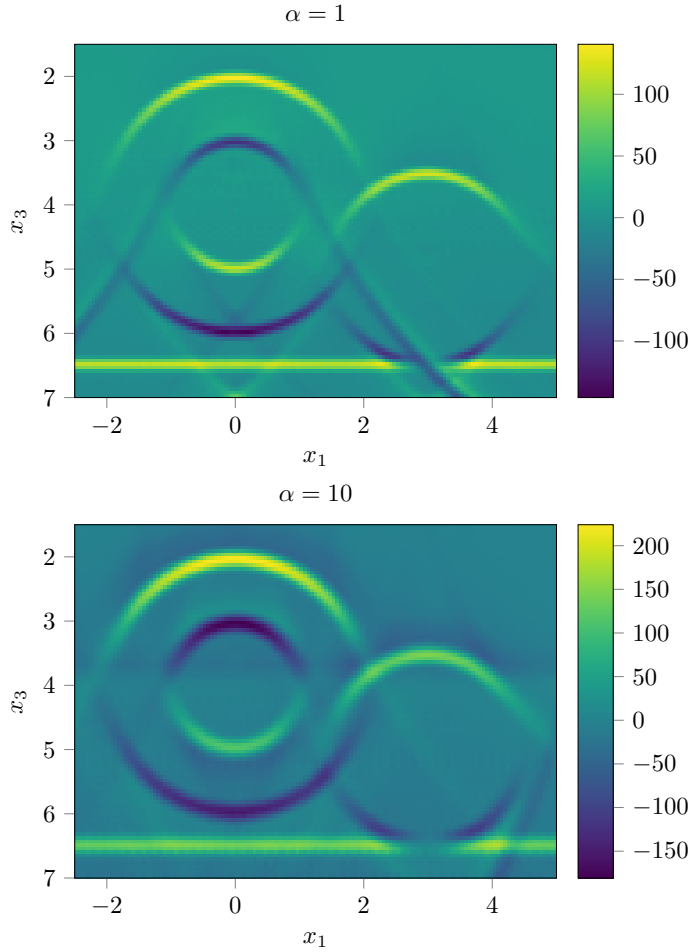
FIGURE 8. Cross section $Q\,L_{\gamma,\mathrm{mod},2}(\cdot,0,\cdot)$ for $\Lambda_{\mathrm{mod},2}$ from (3.10).
Top: $\alpha = 1$ and $\gamma = 0.2$, bottom: $\alpha = 10$ and $\gamma = 0.3$.

occur or are emphasized only when the half space is included. This was confirmed by reconstructions including just the half space and just the balls, and this could be the type of artifact coined "object-independent" in [5, Theorem 5.2]. In addition, some streaks and other image degradation could occur for numerical reasons. Some of these numerical effects are described and named "endpoint artifacts" in [4, Sec. 5.7]. But their cause is only vaguely explained. All these observations suggest that further microlocal analysis needs to be done in future work.

In the next experiment we simulate a situation which very likely occurs in field measurements: the offset is not known exactly and differs slightly from one source/receiver pair to the next. In generating the data we therefore draw a different α for each source/receiver pair randomly and uniformly distributed from $[1.75, 2.25]$. The reconstruction however is done with the mean offset 2, that is, we set $\alpha = 2$ in the reconstruction kernel used in Q (for the values of the other parameters of Q see [10, Sec. 5.3.2]). The result in Figure 10 is a bit blurry but the singular support is still clearly recognizable.
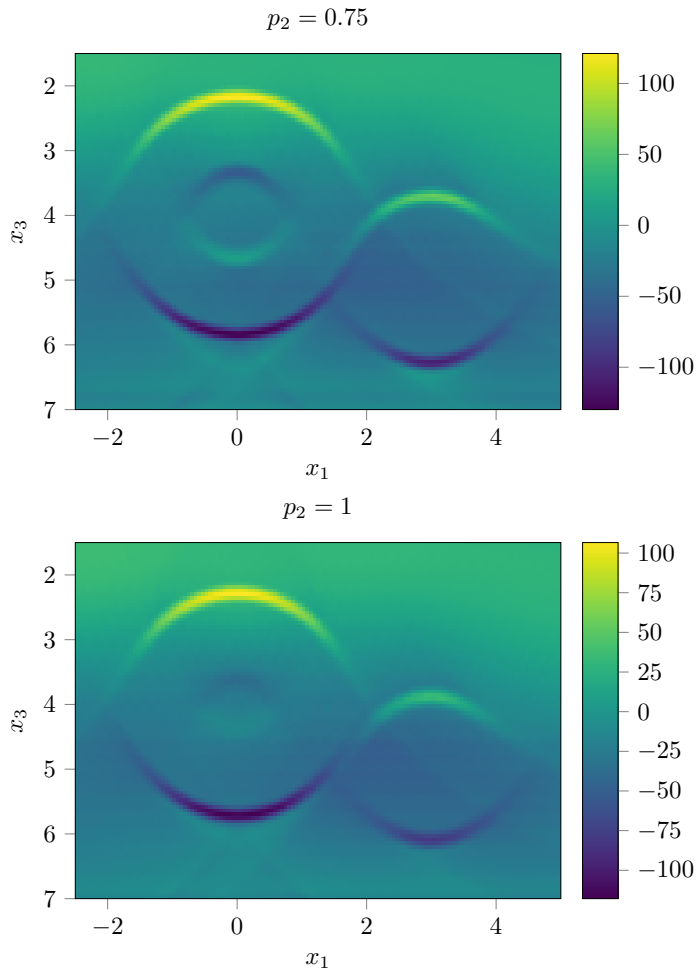
FIGURE 9. Cross sections $Q\, L_{0.2,\mathrm{mod},0} n_*(\cdot, p_2, \cdot)$ for $\Lambda_{\mathrm{mod},2}$ from (3.10) with $\alpha = 1$. Top: $p_2 = 0.75$, bottom: $p_2 = 1$.

Remark 5.1. So far we did not comment on how we selected the scaling/regularization parameter γ, which depends on the discretization step sizes in Q, number of measurements, noise level, and offset. Finding a useful γ is a delicate task indeed. Our explanations and ideas from [11, Rem. 4.1] apply correspondingly.

5.2. **Reconstructions using data from the wave equation.** In the previous experiments we generated data with the same numerical scheme used to evaluate the reconstruction kernels. Here we provide data by solving the acoustic wave equation numerically. Thus, we avoid committing an inverse crime and additionally incorporate the modeling/linearization error, see Section 2.

For generating the data y as in (2.5) we solve the acoustic wave equations (2.1) and (2.3) by the `PySIT` software [13] in the cuboid $[0.1, 0.8] \times [0.1, 1.0] \times [0.1, 0.8]$ with absorbing boundary conditions using perfectly matched layers. The discretization step size is 0.01 and on top of the cuboid 13×35 source and receiver pairs are positioned
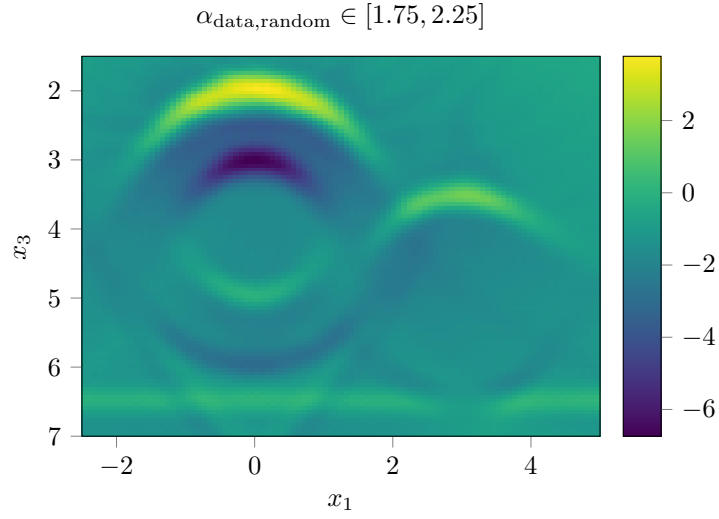
$$\alpha_{\text{data,random}} \in [1.75, 2.25]$$

FIGURE 10. Cross section $Q\,L_{0.4}n(\cdot, 0, \cdot)$ with Λ from (3.1). The offset of the data differs randomly in $[1.75, 2.25]$ for each source/receiver pair whereas the offset in Q is identically 2.
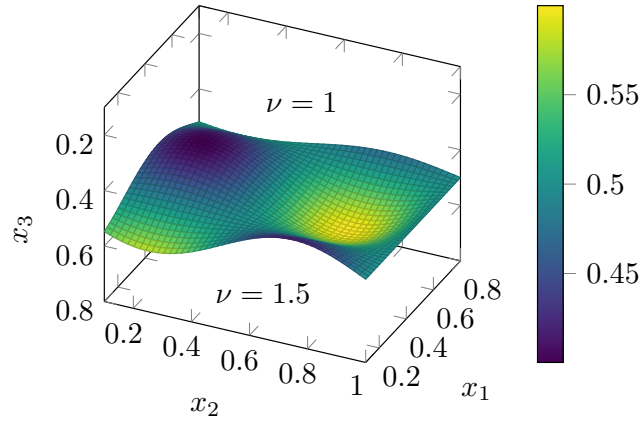

FIGURE 11. An illustration of the speed of sound ν.

at $\mathbf{x}_{\text{s}}(s) = (s_1, s_2 - \alpha, 0.1)^\top$ and $\mathbf{x}_{\text{r}}(s) = (s_1, s_2 + \alpha, 0.1)^\top$ with $s_1 \in \{0.15 + 0.05i \,|\, i \in \{0, \dots, 12\}\}$, $s_2 \in \{0.125 + 0.025j \,|\, j \in \{0, \dots, 35\}\}$, and $\alpha = 0.025$. For the travel time t we take 1709 points between $t_{\min} = 0.1$ and $t_{\max} = 2$ into account. Further, the speed of sound ν in this experiment is

$$\nu(x) = \begin{cases} 1, & \text{if } x_3 \leq 0.1 \sin(2\pi x_2) \cos(2\pi x_1) + 0.5, \\ 1.5, & \text{if } x_3 > 0.1 \sin(2\pi x_2) \cos(2\pi x_1) + 0.5, \end{cases}$$

which simulates two different materials, see Figure 11. The temporal impulse at time $t = 0$, that is, the source is modeled by a scaled and truncated Gaussian.

Figure 12 shows on the left four cross sections of the interface we want to reconstruct. All appearing singularities have a non-vanishing third component in their normal directions, so we expect to see them all in the corresponding reconstructions on the right, which are obtained from (5.2) using the kernel of $\Lambda_{0.07}$ with Λ from (3.1) (the used cutoff function is an adapted version of (5.1)).

In all reconstructed cross sections, the singular support, which is the boundary between the two different material layers, is reconstructed as a relatively thick curve. This is due to a lack of data.

Further, the reconstructed singularities near to the left boundary of the cuboid are less visible than the ones near to the right. The reason is that on the left the first receiver is farther away from the boundary.

If we compare the two cross sections $x_1 = 0.1$ and $x_1 = 0.5$, we notice that all reconstructed singularities in case of $x_1 = 0.5$ have nearly the same intensity whereas for $x_1 = 0.1$ there are big differences. This effect is due to location of the cross sections inside the cuboid. There are more sources and receivers in the middle of the cuboid than at the boundary as there are no pairs of sources and receivers in front of it, i.e., for $x_1 < 0.1$.

At last, we remark that in all four cross sections the strength of the singularities at the boundaries depends on how the interface hits the boundary. By Theorem 3.7 and the consequences of Proposition 3.9, see (5.3) and (5.4) for instance, the imaging operator preserves a singularity of n only if there is an ellipse being integrated over which is tangent to that singularity.

Remark 5.2. In [11, Sec. 4.2] you find a numerical experiment, in 2D though, which takes a further modeling error into account: the required reference solution of the wave equation is not computed with the constant sound speed 1 but with a spatially varying sound speed. This works remarkably well.
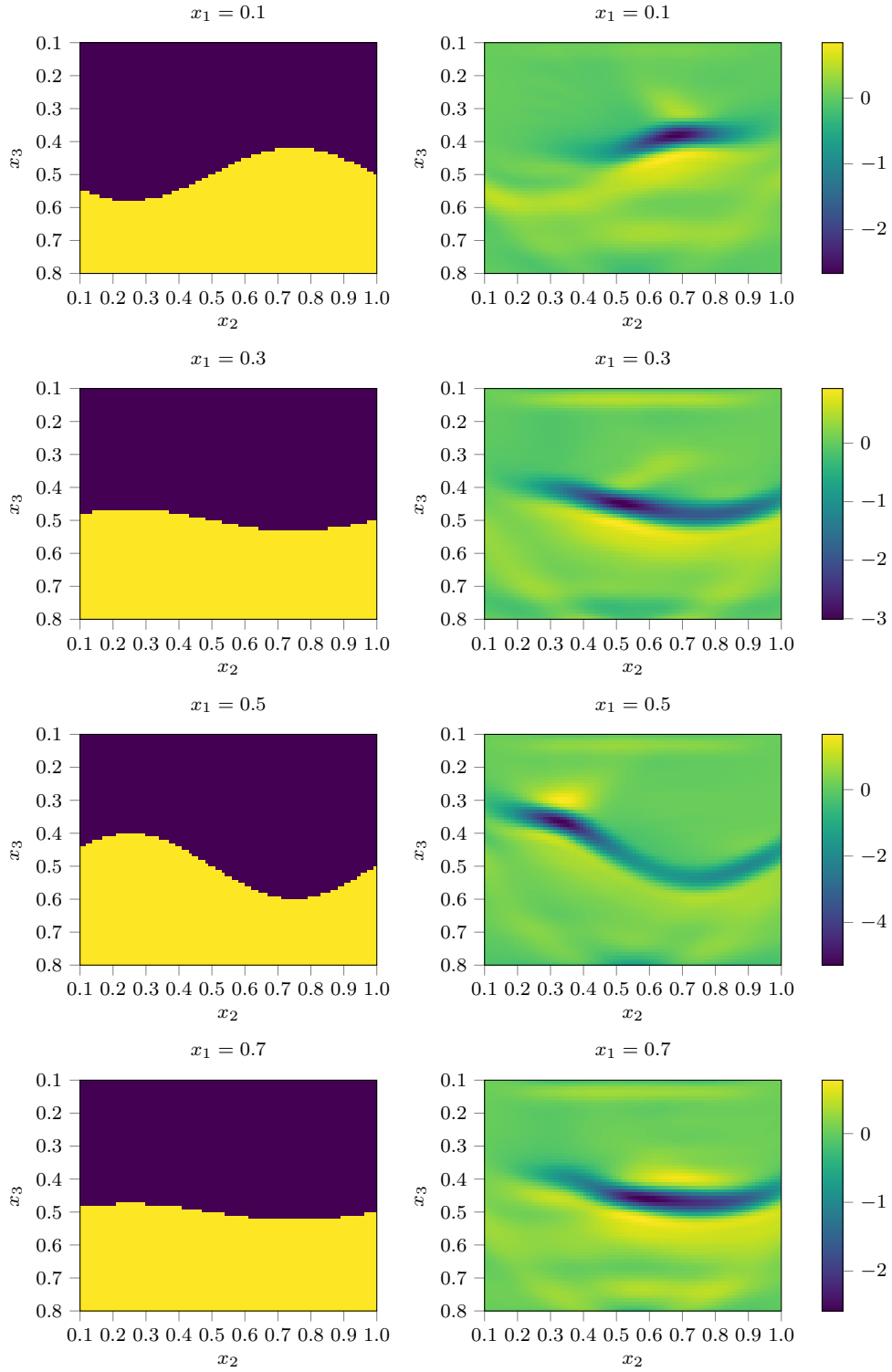
FIGURE 12. Ground truth (left) and the corresponding reconstructions $Q\,L_{0.07}n$ with Λ from (3.1).

References

[1] L.-E. Andersson, *On the determination of a function from spherical averages*, SIAM J. Math. Anal., 19 (1988), pp. 214–232, https://doi.org/10.1137/0519016.

[2] G. Beylkin, *The inversion problem and applications of the generalized Radon transform*, Comm. Pure Appl. Math., 37 (1984), pp. 579–599, https://doi.org/10.1002/cpa.3160370503.

[3] G. Beylkin, *Imaging of discontinuities in the inverse scattering problem by inversion of a causal generalized Radon transform*, J. Math. Phys., 26 (1985), pp. 99–108, https://doi.org/10.1063/1.526755.

[4] N. Bleistein, J. Cohen, and J. J.W. Stockwell, *Mathematics of Multidimensional Seismic Imaging, Migration, and Inversion*, vol. 13 of Interdisciplinary Applied Mathematics, Springer, New York, 2001.

[5] L. Borg, J. Frikel, J. S. Jørgensen, and E. T. Quinto, *Analyzing reconstruction artifacts from arbitrary incomplete X-ray CT data*, SIAM J. Imaging Sci., 11 (2018), pp. 2786–2814, https://doi.org/10.1137/18M1166833.

[6] J. K. Cohen and N. Bleistein, *Velocity inversion procedure for acoustic waves*, Geophysics, 44 (1979), pp. 1077–1085, http://dx.doi.org/10.1190/1.1440996.

[7] M. V. de Hoop, H. Smith, G. Uhlmann, and R. D. van der Hilst, *Seismic imaging with the generalized Radon transform: a curvelet transform perspective*, Inverse Problems, 25 (2009), pp. 025005, 21, http://dx.doi.org/10.1088/0266-5611/25/2/025005.

[8] R. Felea, V. P. Krishnan, C. J. Nolan, and E. T. Quinto, *Common midpoint versus common offset acquisition geometry in seismic imaging*, Inverse Probl. Imaging, 10 (2016), pp. 87–102, https://doi.org/10.3934/ipi.2016.10.87.

[9] J. Frikel and E. T. Quinto, *Artifacts in incomplete data tomography with applications to photoacoustic tomography and sonar*, SIAM J. Appl. Math., 75 (2015), pp. 703–725, https://doi.org/10.1137/140977709.

[10] C. Grathwohl, *Seismic imaging with the elliptic Radon transform in 3D: analytical and numerical aspects*, PhD thesis, Karlsruhe Institute of Technology, 2020, https://doi.org/10.5445/IR/1000105093.

[11] C. Grathwohl, P. Kunstmann, E. T. Quinto, and A. Rieder, *Approximate inverse for the common offset acquisition geometry in 2D seismic imaging*, Inverse Problems, 34 (2018), p. 014002. https://doi.org/10.1088/1361-6420/aa9900.

[12] C. Grathwohl, P. Kunstmann, E. T. Quinto, and A. Rieder, *Microlocal analysis of imaging operators for effective common offset seismic reconstruction*, Inverse Problems, 34 (2018), pp. 114001, 24, https://doi.org/10.1088/1361-6420/aadc2a.

[13] R. J. Hewett, L. Demanet, and The PySIT Team, *PySIT: Python seismic imaging toolbox*, 2020, https://doi.org/10.5281/zenodo.3603367.

[14] L. Hörmander, *Fourier Integral Operators, I*, Acta Mathematica, 127 (1971), pp. 79–183.

[15] V. P. Krishnan, H. Levinson, and E. T. Quinto, *Microlocal analysis of elliptical Radon transforms with foci on a line*, in The Mathematical Legacy of Leon Ehrenpreis, 1930-2010, I. Sabadini and D. Struppa, eds., vol. 16 of Springer Proceedings in Mathematics, Springer, 2012, pp. 163–182, http://dx.doi.org/10.1007/978-88-470-1947-8_11.

[16] A. K. Louis, *Approximate inverse for linear and some nonlinear problems*, Inverse Problems, 11 (1995), pp. 1211–1223, http://stacks.iop.org/0266-5611/11/1211.

[17] C. J. Nolan and W. W. Symes, *Global solution of a linearized inverse problem for the wave equation*, Comm. Partial Differential Equations, 22 (1997), pp. 919–952, https://doi.org/10.1080/03605309708821289.

[18] B. Petersen, *Introduction to the Fourier Transform and Pseudo-Differential Operators*, Pitman, Boston, 1983.

[19] E. T. Quinto, *The dependence of the generalized Radon transform on defining measures*, Trans. Amer. Math. Soc., 257 (1980), pp. 331–346, https://doi.org/10.2307/1998299.

[20] E. T. Quinto, A. Rieder, and T. Schuster, *Local inversion of the sonar transform regularized by the approximate inverse*, Inverse Problems, 27 (2011), p. 035006 (18p), https://doi.org/10.1088/0266-5611/27/3/035006.

[21] Rakesh, *A linearised inverse problem for the wave equation*, Comm. Partial Differential Equations, 13 (1988), pp. 573–601, https://doi.org/10.1080/03605308808820553.

[22] M. A. Shubin, *Pseudodifferential operators and spectral theory*, Springer Series in Soviet Mathematics, Springer-Verlag, Berlin, 1987. Translated from the Russian by Stig I. Andersson.

[23] C. C. STOLK, *Microlocal analysis of a seismic linearized inverse problem*, Wave Motion, 32 (2000), pp. 267–290, `https://doi.org/10.1016/S0165-2125(00)00043-3`.

[24] W. W. SYMES, *Mathematics of reflection seismology*, tech. report, The Rice Inversion Project, Rice University, Houston, TX, USA, 1998, `http://www.trip.caam.rice.edu/downloads/preamble.pdf`.

DEPARTMENT OF MATHEMATICS, KARLSRUHE INSTITUTE OF TECHNOLOGY (KIT), D-76128 KARLSRUHE, GERMANY

E-mail address: `christine.grathwohl@kit.edu`

E-mail address: `peer.kunstmann@kit.edu`

E-mail address: `andreas.rieder@kit.edu`

DEPARTMENT OF MATHEMATICS, TUFTS UNIVERSITY, MEDFORD, MA 02155, USA

E-mail address: `todd.quinto@tufts.edu`